

https://dspace.org/

Microstructure, hardness, oxidation and corrosion behavior of Cr(VNb)2 Laves containing CrNbTaVW RHEA in 3.5 wt% NaCl and 1 M H2SO4

Olufemi Bamisaye; Nthabiseng Maledi; Josias Van Der Merwe; Michael Bodunrin

https://hdl.handle.net/10539/40530
WOS

Downloaded from a DSpace repository. https://dspace.org/

International Journal of Refractory Metals and Hard Materials 121 (2024) 106661



Contents lists available at ScienceDirect

International Journal of Refractory Metals and Hard Materials

journal homepage: www.elsevier.com/locate/IJRMHM





Microstructure, hardness, oxidation and corrosion behavior of $Cr(VNb)_2$ Laves containing CrNbTaVW RHEA in 3.5 wt% NaCl and 1 M H_2SO_4

Olufemi Sylvester Bamisaye [a,c,*], Nthabiseng Maledi [a,b], Josias Van der Merwe [a,b], Michael Oluwatosin Bodunrin [a,b]

[a] School of Chemical and Metallurgical Engineering, Faculty of Engineering and the Built Environment, University of the Witwatersrand, Johannesburg, South Africa
[b] DSI-NRF Centre of Excellence in Strong Materials, University of the Witwatersrand, Johannesburg, South Africa
[c] Mechanical Engineering Department, Faculty of Air Engineering, Air Force Institute of Technology, Kaduna, Nigeria

ARTICLE INFO

Keywords:
Laves phase strengthening
Multi-phase RHEA
Corrosion resistance
Thermal stress
Growth stress
Oxidation properties

ABSTRACT

In this study, CrNbTaVW RHEA was produced via vacuum arc melting. The microstructure, hardness, corrosion and oxidation properties were explored in comparison with the commercial IN718 alloy. The results indicated that CrNbTaVW RHEA exhibited a dendritic microstructure that was segregated into BCC1, BCC2, and $Cr(VNb)_2$ Laves. The CrNbTaVW RHEA has a higher hardness of 688 HV than the IN718 alloy with 301 HV. The higher hardness is due to Laves phase solid solution strengthening and grain refinement. From the corrosion results, CrNbTaVW RHEA had a lower corrosion rate in 3.5 wt% NaCl (0.000097 mm/yr) and 1 M H_2SO_4 (0.00013 mm/yr) than the commercial IN718 alloy (0.054 mm/yr and 1.12 mm/yr). The cyclic oxidation analysis at 850 °C and 1050 °C after 15 hours confirmed a mass gain of 4.41 mg/cm^2 and 10.84 mg/cm^2 for IN718 alloy, while CrNbTaVW RHEA exhibited a mass loss of −25.17 mg/cm^2 and − 35.91 mg/cm^2, respectively, indicating that the IN718 alloy exhibited the best oxidation resistance. Thermal and growth stresses contributed to the pores, voids, cracks, and spallation observed in the CrNbTaVW RHEA.

1. Introduction

The development of new functional materials, metals, and alloys has been the primary driving force behind the progression of human civilization. In 2004, Cantor et al. [1] and Yeh et al. [2] first reported high entropy alloy (HEA) as a type of novel structure material that demonstrated superior properties to those of conventional alloys. The HEAs have exceptional mechanical properties, such as strength, hardness, high temperature phase stability, improved wear, corrosion, and oxidation resistance [1,3,4]. Refractory high entropy alloy (RHEA) which comprise mostly groups IV, V, and VI elements have also been developed and considered as potential high temperature structural materials for applications such as nuclear reactors, heat exchanger tubing, and rocket engine nozzles [5,6]. The RHEAs provide a unique opportunity in the area of alloy design by raising the temperature capability against conventional alloying strategies and improving corrosion and oxidation resistance. The elemental addition of elements such as Ta, W, Cr, V, Nb can significantly influence the mechanical properties of RHEAs [7–10]. Most especially, Cr forming Laves phase that have been reported to significantly enhance the mechanical properties of RHEAs [11–13]. Fang et al. [12] found an increase in hardness (567 HV) and compressive strength (1389 MPa) for $ZrNbTaHf_{0.2}Cr_x$ RHEA due to the volume fraction of the C15_Laves phase. Xiang et al. [14] reported the hardness and compressive strength of MoNbFeCrV to be 827 HV and 2688 MPa and MoNbFeCrTi RHEA to be 792 HV and 1811 MPa respectively, due to the formation of the C15_Laves phase.

Despite the increase in hardness and compressive properties, limited work has focused on the corrosion resistance of RHEAs in chloride and acidic environments. Corrosion is the degradation of materials that occurs as a result of electrochemical reactions between the material and the environment [15]. In materials design, elemental addition might affect the corrosion performance by altering the structure of the phase, multiphase and element segregation, reducing the passivity and nobility of the phases, and influencing the dissolution kinetics [16]. Studies on the corrosion behavior of single-phase RHEA in acidic and chloride solutions have been investigated [17–19]. Zhou et al. [20] investigated the

* Corresponding author at: School of Chemical and Metallurgical Engineering, Faculty of Engineering and the Built Environment, University of the Witwatersrand, Johannesburg, South Africa.
E-mail addresses: 2503285@students.wits.ac.za, bamisayesylvester1988@gmail.com (O.S. Bamisaye).

https://doi.org/10.1016/j.ijrmhm.2024.106661
Received 4 December 2023; Received in revised form 16 March 2024; Accepted 19 March 2024
Available online 21 March 2024
0263-4368/© 2024 The Authors. Published by Elsevier Ltd. This is an open access article under the CC BY-NC-ND license (http://creativecommons.org/licenses/by-nc-nd/4.0/).

corrosion resistance of $Hf_{0.5}Nb_{0.5}Ta_{0.5}Ti_{1.5}Zr$ RHEA in chloride solution and found the alloy to have better corrosion resistance than that of 316 L stainless steel, due to formation of a single phase and passivation promoting elements. Gao et al. [21] found single BCC phase $Mo_{0.5}Nb_{20}Ta_{10}Ti_{35}V_{20}$ RHEA to have better corrosion resistance than that of 316 L stainless steel in chloride solution. Open pits were found in single phase $TiCrVNb_{0.5}Al_{0.5}$ RHEA when exposed to acidic solution [22]. This means like all commonly used corrosion resistant alloys; single phase RHEAs can also undergo localized pitting corrosion. For the dual-phase RHEAs, Xiang et al. [14] studied the corrosion behavior of dual phase (BCC and V-rich sigma phase) MoNbFeCrV RHEA and found only the V-rich sigma phase to be preferentially dissolved when exposed to acidic solution. Bi et al. [23] studied the corrosion behavior of dual phase (BCC and Zr_5Al_3) AlNbTiZr RHEA and found preferential corrosion and pitting within the Zr_5Al_3 phase regions when exposed to chloride solution. However, corrosion studies on dual-phase and multi-phase RHEA containing C15_Laves phase in chloride and acidic solution have not been reported so far. Hence, it is important for the corrosion performance of dual-phase and multi-phase RHEA containing C15_Laves phases to be evaluated to determine their functionality in chloride and acidic environments.

Oxidation resistance is a vital property for alloys working for a long time at high temperatures since it can severely deteriorate the mechanical properties of the materials. The oxidation resistance of the alloys is affected by the compactness of the oxide scale, which can be described through the Pilling−Bedworth ratio (PBR) [24]. According to Lekakh et al. [25], the oxide layer adhesion to the steel substrate depends on various parameters: scale thickness, growth rate, stress rate, interfacial energy, and elastic properties of the oxide. In many applications, oxide scale may fail due to various external loads that may lead to cracking and spalling of the oxide scale and ultimately to exposure of the bare-metal surface [26]. The cyclic-oxidation behavior is more complicated than isothermal oxidation because of the spalling process during cooling [26]. Most oxidation studies of RHEAs are conducted in isothermal conditions rather than in cyclic conditions [27–31]. These have made it difficult to study the spallation behavior of RHEAs when exposed to high temperatures. Furthermore, the effect of growth stress and thermal stress on the formation of holes and cracks in oxidized RHEAs has not been fully reported.

In this study, the empirical parameters of entropy of mixing, enthalpy of mixing, valence electron concentration, lattice distortion, electronegativity difference, and thermodynamic parameter were used to design, predict the phases and stability of an equiatomic CrNbTaVW RHEA. Second phase hardening such as the addition of Cr have been reported to induce a Laves phase for increased hardness [11,32,33]. The addition of V has been reported to enhance the mechanical properties of RHEAs due to grain refinement [34]. V has been reported to protect RHEAs from localized corrosion, such as pitting, in NaCl and H_2SO_4 solutions [35]. The addition of Nb, W, and Ta has been reported to reduce the rate of dissolution of materials [36,37]. The alloys containing W, Cr, Nb have strong passivation potentials, which enable oxide films to form in HEAs with compact packing structures [14,38–40]. The high diffusion of Cr can enable the synthesis of $CrTaO_4$, Cr_2O_3, and $CrNbO_4$ that would form a barrier for both inward diffusion of oxygen and outward diffusion. These will provide protection against oxidation at high temperatures [41–44].

Hence, this study developed and investigated the microstructure, hardness, corrosion, and oxidation properties of multiphase CrNbTaVW RHEA and compared them with the commercial IN718 nickel-based superalloy. The corrosion mechanism of the multiphase RHEA was explained in 3.5 wt% NaCl and 1 M H_2SO_4. The oxidation mechanism of the multiphase RHEA was further elucidated after 15 hours exposure. This study is expected to provide more information on the microstructure, hardness, corrosion, and oxidation properties of multiphase RHEA.

2. Experimental procedures

2.1. Material preparation

Metallic powders (Cr, Nb, Ta, V, and W) with purity >99.7 wt% purchased from Weartech Pty Limited, South Africa, were melted and solidified by a vacuum arc melting furnace in a high purity argon atmosphere on a water-cooled Cu hearth to obtain CrNbTaVW RHEA samples. The samples were turned and remelted three times to ensure chemical homogeneity. A commercial IN718 super alloy was also obtained. The CrNbTaVW RHEA and commercial IN718 super alloy samples were cut to precision using Gold San CNC wire cutting EDM machine operating at 20 V. The sectioned samples were hot mounted in phenolic resin (Struers Polyfast) using a Bainmount twin H auto hot mounting press at a temperature of 160 °C and a pressure of 150 bar. The mounted samples were automatically grounded on the Struers Tegramin-20 grinding machine using Struers MD-Piano 2000 and Struers MD-Piano 4000 resin bonded diamond grinding discs. After the grinding operation, the samples were polished using Akasel polishing cloth, with 3 μm two-in-one polycrystalline diamond suspension.

2.2. Hardness testing

Vickers hardness tests were conducted on polished cross-sectional area of the CrNbTaVW RHEA and IN718 alloy samples using a FutureTech Vickers hardness tester (FM-800) equipped with a diamond indenter. The measurements were taken under a load of 300 gf and a dwell time of 15 s for CrNbTaVW RHEA and IN718 alloy according to ASTM standard E92–17 [45]. Ten readings were taken at different positions on samples to obtain the average of the Vickers hardness.

2.3. Corrosion testing

The sectioned CrNbTaVW RHEA and IN718 alloy samples were hot mounted in clear resin at a temperature of 180 °C and a pressure of 150 bar, ground, and polished until a mirror-like finish was obtained. After polishing, the samples were rinsed in water and air-dried. The samples, with a surface area of 0.283 cm^2 were subjected to the corrosive solutions. The corrosion test was performed using a three-electrode electrochemical cell connected to a Gamry® potentiostat. CrNbTaVW RHEA and IN718 alloy samples was used as the working electrode, while a platinum wire and Ag/AgCl saturated with 3 M KCl solution were used as the counter and reference electrodes, respectively. Open circuit potential (OCP) test in 3.5 wt% NaCl and 1 M H_2SO_4 solutions was conducted for 3600 s after immersion in the solutions to reach a stable value. Afterwards, potentiodynamic polarization tests were performed at a scan rate of 0.167 mV/s in the potential range of −0.5 to 2.5 V at room temperature. The corrosion current density (I_{corr}), corrosion potential (E_{corr}), and corrosion rate were determined using the polarization technique according to ASTM standard G59–97 [46].

2.4. Oxidation testing

The CrNbTaVW RHEA and IN718 samples for the oxidation tests were sectioned using a Gold San CNC wire cutting EDM machine to nominal dimensions of $6 \times 6 \times 7$ mm^3. The surfaces of the samples were ground using SiC papers grade to P1200, cleaned in an ultrasonic acetone and then dried in air. Afterwards, oxidation test was carried out in an open-ended tube muffle furnace under laboratory air at 850 °C and 1050 °C for 15 hours. The mass changes of the alloy samples before and after oxidation was measured using a Boeco digital weighing balance (accuracy = 0.0001 g) to characterize the oxidation kinetics.

2.5. Composition and microstructure analysis

The microstructural analysis of the samples was examined using a

high-resolution Zeiss Sigma Field Emission Scanning Electron Microscope (FEG-SEM) in secondary electron (SE) and backscattered electron (BSE) detectors at 20 kV. The microstructure of the samples after the corrosion test, surface and cross-sectional morphology of the oxidized samples were also examined using FEG-SEM. SEM was also used in combination with energy dispersive X-ray (EDX) for elemental compositions. Image J software (Open-source software for image analysis, National Institutes of Health) was used to calculate the grain size, pores, voids, and cracks. The phase identification of the samples, corrosion products, and oxides were examined using a Bruker D2 phase diffractometer, with a Co Kα radiation source [λ = 1.78899 Å] at 30 kV and a current of 25 mA within the range of 2θ = 20–120° at a temperature of 25 °C.

3. Results

3.1. Microstructure and phase analysis of CrNbTaVW and IN718

The phases and microstructure present in the as-cast CrNbTaVW RHEA and IN718 were identified by XRD analysis and SEM, as presented in Fig. 1. The XRD analysis result of the CrNbTaVW RHEA shows the peaks are indexed as two BCC solid solution phases and $Cr(VNb)_2$ C15-Laves phase (Fig. 1a). The BCC 1 structure is the primary phase (Im-3 m (229); a = b = c = 3.1980; reference: 96–900-6501), BCC 2 structure is the secondary phase (Im-3 m (229); a = b = c = 3.0240; reference: 96–901-2771), and the $Cr(VNb)_2$ C15-Laves phase (Fd-3 m (227); a = b = c = 7.0790; reference: 96–152-3579). SEM images of CrNbTaVW in Figs. 1(b) and (c) showed that the alloy exhibited a dendritic microstructure that segregated into a white phase (BCC1), grey phase (BCC2), and dark phase ($Cr(VNb)_2$). BCC and Laves phases have been reported in some Cr containing as-cast RHEAs, for example, CrNbTiZr RHEA [47] and CrHfNbTaTi [48]. According to Butler et al. [49], Laves particles precipitated inside grains during cooling in the solid state due to decreasing Cr solubility in the BCC phase. During the nucleation and growth of a new phase, the coordinated diffusion of several elements is important because it requires the redistribution of all elements to reach the desired composition [50]. The average grain size of the dendrites and the Laves phase is 47.3 ± 2.1 μm and 11 ± 0.7 μm respectively. The XRD results in Fig. 1(d) showed that two major phases are present in IN718 alloy, namely, the γ phase (FeMnNi) with space group Fm-3 m (225) and lattice parameter (a = b = c = 3.2350 Å) and the γ'' phase of Ni_3Nb (Fm-3 m (225); a = b = c = 3.6150). The microstructure of the IN718 alloy has uniformly distributed ($\gamma + \gamma''$) phases (Fig. 1e). According to Ganji and Rajyalakshmi [51], the γ phase is soft in nature, while the γ''phase is the main strengthening phase in most precipitation hardenable nickel base super-alloys.

Table 1 shows the chemical composition of CrNbTaVW RHEA. It was found that the higher melting point elements of W and Ta segregated in the dendritic region (BCC1), while lower melting point elements of V and Cr segregated more in the inter-dendritic regions of (BCC2) and Cr $(VNb)_2$ Laves phase. Nb is distributed evenly in both the dendritic and inter-dendritic regions. This highlights the influence of melting points on segregation that is typical in as-cast alloys. The chemical composition of IN718 alloy is presented in Table 2. It can be seen that the IN718 alloy in this study has a higher composition of Fe than Ni.

Table 1
Composition distribution of the CrNbTaVW RHEA (at. %).

Element	Cr	Nb	Ta	V	W
Actual	16 ± 0.5	22 ± 0.2	21 ± 0.2	22 ± 0.2	19 ± 0.9
BCC1	8 ± 0.4	19 ± 0.4	26 ± 0.6	17 ± 1.1	30 ± 1.4
BCC2	32 ± 1.2	20 ± 0.4	13 ± 0.5	30 ± 0.8	5 ± 0.6
$Cr(VNb)_2$ Laves	34 ± 2.1	19 ± 0.9	11 ± 0.3	33 ± 1.5	3 ± 0.5

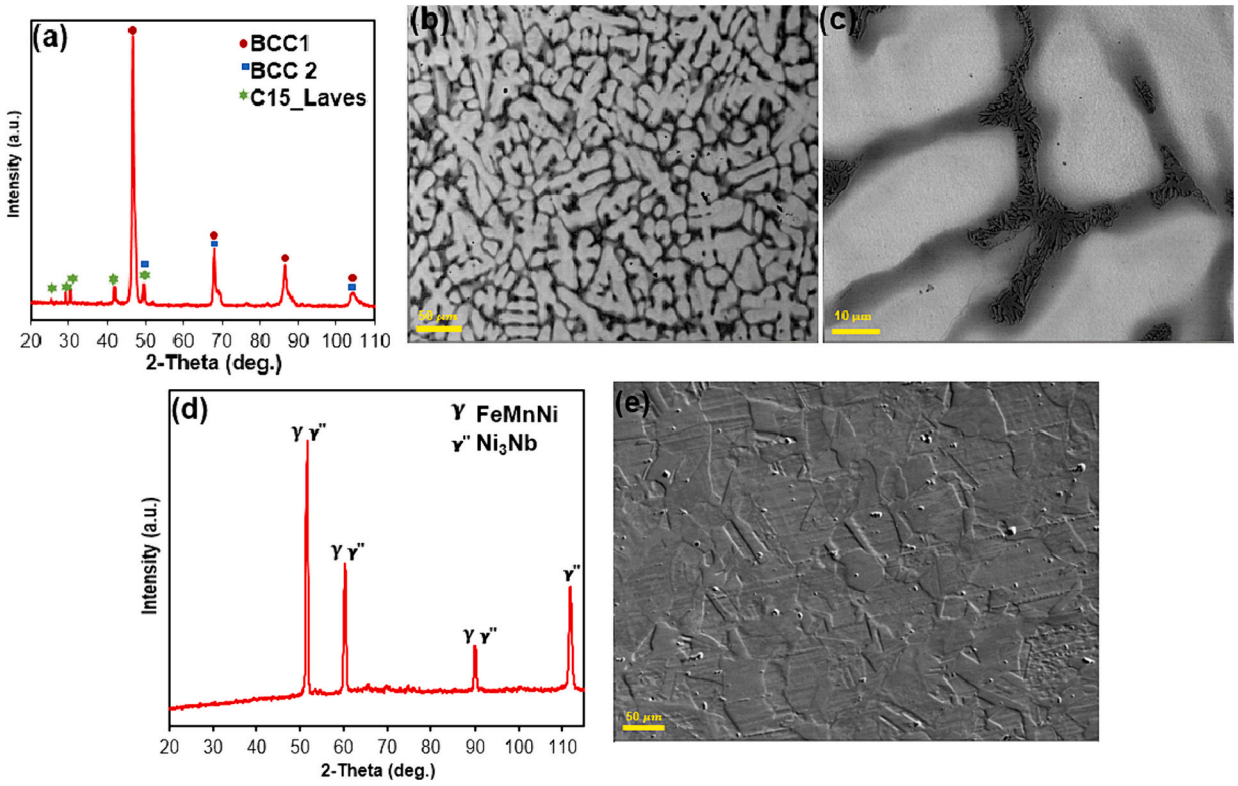


Fig. 1. Phase composition of the CrNbTaVW RHEA showing BCC1, BCC2, and $Cr(VNb)_2$ C15-Laves phase (a); Dendritic microstructure of the CrNbTaVW RHEA (b); Higher magnification image of the CrNbTaVW RHEA showing BCC1, BCC2, and $Cr(VNb)_2$ C15-Laves phase (c); Phase composition of the IN718 alloy showing $\gamma + \gamma''$ phases (d); Microstructure of the IN718 alloy showing $\gamma + \gamma''$ (e).

Table 2
Composition distribution of the IN718 alloy (at. %).

Ti	Nb	Fe	Ni	Mn	S	C	Co	Al	Si	P	Cu
0.12 ± 0.02	0.22 ± 0.02	57.95 ± 0.1	36.56 ± 0.4	0.5 ± 0.1	0.06 ± 0.1	3.63 ± 0.1	0.14 ± 0.04	0.12 ± 0.02	0.37 ± 0.02	0.1 ± 0.01	0.23 ± 0.01

3.2. Hardness properties of CrNbTaVW

The hardness test result of CrNbTaVW RHEA after ten indentations is 688 ± 21 HV, which is higher than IN718 (301 ± 14 HV). The CrNbTaVW RHEA has higher hardness than some reported as-cast RHEAs: CrMoTaTi (630 HV) [11], WNbMoTaZr (557 HV) [52], TiMoNbZr$_{0.5}$ (516 HV) [53], and Hf$_{0.25}$NbTaW$_{0.5}$ RHEA (514 HV) [33]. The higher hardness can be attributed to Laves phase solid solution strengthening and grain refinement. Grain refinement by the elemental addition of V can contribute to finer grain size that has a significant influence on hardness. For example, grain size refinement was achieved in WNbMoTaV RHEA and V$_1$NbMoTa RHEA due to the strong solute effect of V, which contributed to growth restrictions [5,54]. Furthermore, grain growth can be restricted by Cr(VNb)$_2$ Laves phase precipitation in the microstructure, which reduces grain size, and improve hardness. The increased Cr composition to form the Cr(VNb)$_2$ Laves phase in CrNbTaVW RHEA thus led to solid solution strengthening, which further enhanced the hardness. The presence of the Cr promoting Laves phase have been reported to increase the hardness properties of RHEAs [11,13].

3.3. Electrochemical corrosion behavior

3.3.1. Open circuit potential, potentiodynamic polarization measurement, and microstructural observation of CrNbTaVW and IN718 in chloride solution

The OCP and potentiodynamic polarization curves of CrNbTaVW RHEA and IN718 alloy in 3.5 wt% NaCl are presented in Fig. 2. The stability of the oxide film formed on the surface of the CrNbTaVW RHEA and IN718 alloy was evaluated by OCP for 3600 s, as seen in Fig. 2(a). The OCP curve of CrNbTaVW RHEA is stable throughout immersion, which indicates a stable passive film. The OCP curve of the IN718 alloy exhibited several oscillations until 3600 s, which can be attributed to the dissolution and re-passivation of the oxide films formed on the alloy surface [20,55]. These results suggest that CrNbTaVW RHEA oxide film is more stable than the IN718 alloy in a 3.5 wt% NaCl solution. Stable OCP has been attributed to the building of compact and protective oxide films on alloy surfaces [56,57]. The potentiodynamic polarization curves of the CrNbTaVW RHEA and IN718 alloy in 3.5 wt% NaCl after the OCP test are presented in Fig. 2(b). It was observed that the anodic curve of CrNbTaVW RHEA exhibited a wide passivation region up to the final potential of 2.5 V, which indicates that the passive film of CrNbTaVW RHEA is stable and good. The polarization curve of the IN718 alloy exhibited pseudo-passive behavior up to 1.63 V and later passivated until the final potential. Active corrosion took place when the IN718 alloy was exposed to a chloride solution, which is identified by the red arrow in the anodic curve. The Cl^- ions attacked the protective layer, breaking the passive layer. However, the oxide layer was rebuilt as evidenced by the pseudo-passive and passive behaviors. The electrochemical corrosion parameters such as E_{corr}, I_{corr}, and corrosion rates obtained from the polarization curve in a 3.5 wt% NaCl solution are presented in Table 3. The CrNbTaVW has a higher negative E_{corr} value of −0.139 V than the IN718 with −0.295 V, which indicates its susceptibility to corrosion. The CrNbTaVW RHEA has a lower I_{corr} value of 0.0026 μA/cm^2 than the IN718 alloy with 5.299 μA/cm^2. Based on the corrosion parameters, it is obvious that the CrNbTaVW RHEA show a very low corrosion rate in 3.5 wt% NaCl compared to the IN718 alloy.

The SEM images and XRD of the CrNbTaVW RHEA and IN718 alloys after potentiodynamic polarization in 3.5 wt% NaCl are presented in Fig. 3. Pits with an average size of 2.43±0.4 μm and corrosion products were observed on the surface of CrNbTaVW RHEA (Fig. 3a and b). The IN718 alloy surface is highly corroded, and pits of an average size of 14.86±2.2 μm were seen in different regions (Fig. 3c). Corrosion products were also seen in corroded and non-corroded areas of the IN718 alloy surface. The EDX compositions obtained from the regions of the IN718 alloy and CrNbTaVW RHEA after potentiodynamic polarization

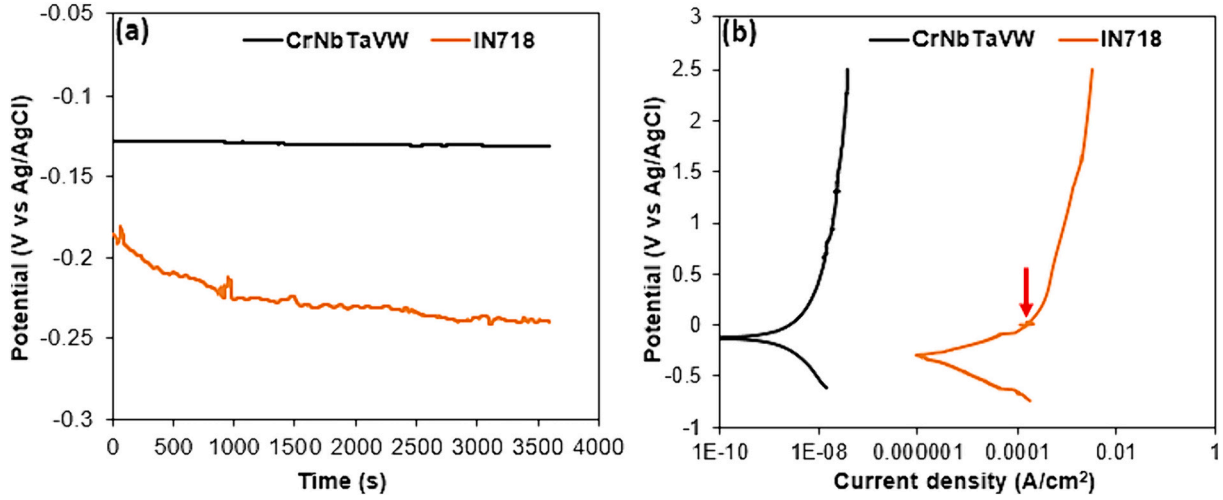


Fig. 2. OCP and polarization curves for CrNbTaVW RHEA and IN718 alloy in 3.5 wt% NaCl solution at room temperature: (a) OCP curves of CrNbTaVW RHEA and IN718 alloy for 3600 s. (b) Potentiodynamic polarization curves for CrNbTaVW RHEA and IN718 alloy.

Table 3
Electrochemical parameters for CrNbTaVW and IN718 in 3.5 wt% NaCl.

Alloy	E_{corr} (V)	I_{corr} (μA/cm^2)	Corrosion rate (mm/yr)
CrNbTaVW	−0.139 ± 0.011	0.0026 ± 0.001	0.000097 ± 0.0008
IN718	−0.295 ± 0.01	5.299 ± 2.06	0.054 ± 0.02

in 3.5 wt% NaCl are presented in Supplementary Table 1 and Supplementary Figs. 1 and 2. The presence of oxygen was observed in the alloys, which implies oxide formed on the surface of the CrNbTaVW RHEA and IN718 alloys. The deposition of Cl element in the compositions signified the presence of Cl^- which broke through the oxide layer of the IN718 alloy and led to the corroded surface and pits. Also, Cl^- broke through the passive layer of CrNbTaVW alloy and led to a few smaller pits.

The CrNbTaVW RHEA did not show dissolution of elemental composition in both the dendrite and interdendrite regions (Supplementary Table 1). The addition of V protects RHEAs from localized corrosion, such as pitting in NaCl and H_2SO_4 solutions [58]. Despite substantial amount of V and almost evenly distributed Nb compositions in all the three phases, few pits were still observed at the RHEA surface. It was found that low W and Ta compositions were observed at BCC1 and

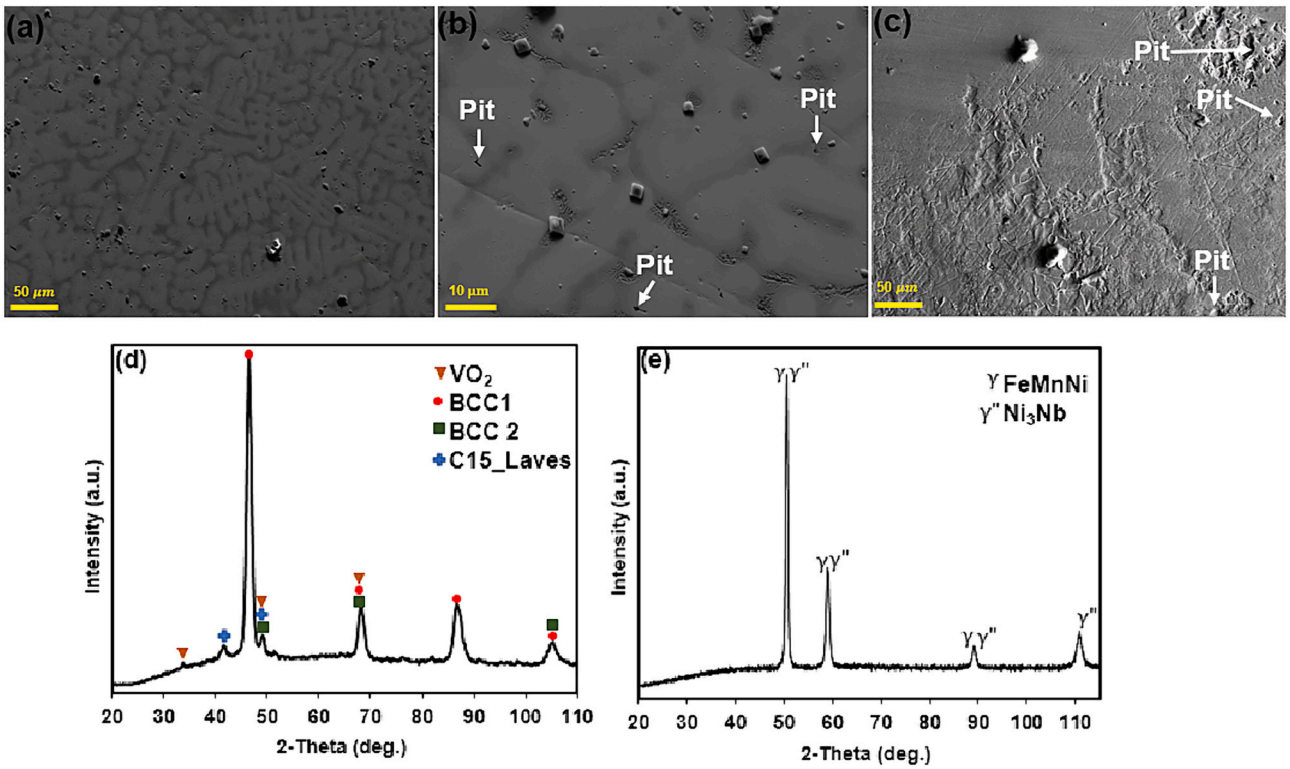


Fig. 3. Surface morphology of the CrNbTaVW RHEA after exposure in 3.5 wt% NaCl (a); Higher magnification image of the CrNbTaVW RHEA surface showing pits after exposure in 3.5 wt% NaCl (b); Surface morphology of corroded surface and pits formed on the IN718 after exposure in 3.5 wt% NaCl (c); Phase analysis of corrosion products present in the CrNbTaVW RHEA (d); Phase analysis of corrosion products present in the IN718 alloy (e).

$Cr(VNb)_2$ phases, which suggest that elemental segregation might have played a role in the formed pits. X-ray diffraction analysis in Fig. 3(d) identified the corrosion product formed on the CrNbTaVW RHEA to be VO_2. All the initial phases are still present, suggesting that no preferential phase dissolution occurred in the CrNbTaVW RHEA when exposed to a chloride solution. The XRD pattern of the IN718 alloy after potentiodynamic polarization showed a reduction of peaks between 60° and 110° (Fig. 3e) that differed from initial phase peaks. It was also observed that no new peaks were formed, which shows that limited oxides were deposited on the IN718 alloy surface. Therefore, no protection was offered and this led to a corroded surface and pits when exposed to 3.5 wt% NaCl solution.

3.3.2. *Open circuit potential, potentiodynamic polarization measurement, and microstructural observation of CrNbTaVW and IN718 in acidic solution*

The stability of the oxide film formed on the surface of the CrNbTaVW RHEA and IN718 alloys was evaluated by OCP for 3600 s in 1 M H_2SO_4 is presented in Fig. 4. The OCP curve of CrNbTaVW RHEA in Fig. 4(a) showed an initial increase in OCP but later dropped in potential to 2586 s. Afterwards, stability was achieved in the OCP for 3600 s at −0.17 V. In the IN718 alloy, the OCP curve is noticeably unstable. Fluctuations were seen in both alloys, suggesting the breaking and rebuilding of the oxide film on the alloy surface. The potentiodynamic polarization curve of the CrNbTaVW RHEA and IN718 alloy in 1 M H_2SO_4 after the OCP test is presented in Fig. 4(b). Active dissolution and pits (indicated by red circle) were observed in the anodic curve of CrNbTaVW RHEA at 0.18 V to 0.46 V and later passivated to a final potential of 2.5 V. The IN718 alloy polarization curve exhibited active corrosion, passivation, and transpassivation. Sulphate ions attack the protective layer of the CrNbTaVW RHEA and IN718 alloy, causing the oxide layer to break. However, the oxide layer begins to repair as seen in the passivation region (Fig. 4b). The electrochemical corrosion parameters such as E_{corr}, I_{corr}, and corrosion rates obtained from the polarization curve in 1 M H_2SO_4 solution are presented in Table 4. It is evidenced from the electrochemical parameters that the corrosion rate of CrNbTaVW RHEA is lower than the IN718 alloy in acidic environment.

The SEM images and XRD analysis of the CrNbTaVW RHEA and IN718 alloy after potentiodynamic polarization in 1 M H_2SO_4 are presented in Fig. 5. Deposits of corrosion products were seen on different regions of the CrNbTaVW RHEA surface (Fig. 5a and b). At higher resolution, pits of an average size of 2.46 ± 0.23 μm were found at BCC1 (white region) of the CrNbTaVW RHEA surface, suggesting that the sulphate ions broke the oxide films (Fig. 5b). The IN718 alloy surface also corroded with circular pits of average size of 6.27 ± 0.68 μm (Fig. 5c and d). The EDX compositions of the IN718 alloy and CrNbTaVW RHEA after polarization in 1 M H_2SO_4 are presented in Supplementary Table 2 and Supplementary Figs. 3 and 4. The presence of oxygen was observed in the compositions of both alloys suggesting oxide formation.

Table 4
Electrochemical parameters for CrNbTaVW RHEA and IN718 alloy in 1 M H_2SO_4.

Alloy	E_{corr} (V)	I_{corr} (μA/cm^2)	Corrosion rate (mm/yr)
CrNbTaVW	−0.147 ± 0.02	0.0039 ± 0.01	0.00013 ± 0.00012
IN718	−0.377 ± 0.01	104.59 ± 4.01	1.12 ± 0.001

In the CrNbTaVW RHEA, BCC1 which was segregated in the dendritic region still retained a substantial amount of Nb, Ta, V, W but lower Cr compositions. BCC2 in the interdendritic region still retained a substantial amount of Cr, Nb, and V but lower W and Ta compositions. The $Cr(VNb)_2$ C15-Laves phase dissolved after corrosion exposure in 1 M H_2SO_4 (Fig. 5b). This might be correlated with the OCP in Fig. 4(a), where there was a rapid increase in the potential and oscillations due to the dissolution and rebuilding of the oxide film on the alloy surface. Elemental segregation of Cr in the dendrite region and segregation of Ta and W in interdendrite region might play a role in the pits and phase dissolution that was observed. Selective dissolution of Cr_2Nb Laves phases was observed in CrMoNbWV HEA in the 0.5 M H_2SO_4 solution [59]. The formation and dissolution behavior of the film in an acidic solution was also observed for Cr containing $AlCoCrFeNi_{2.1}$ HEA [60]. Also, selective dissolution of the V-rich Sigma phase was also reported in a MoNbFeCrV RHEA after the potentiodynamic polarization test in 0.5 M H_2SO_4 solution [14].

XRD analysis in Fig. 5(e) identified the corrosion product formed on the CrNbTaVW RHEA to be VO_2. BCC1 and BCC2 phases are still present, while the peaks of $Cr(VNb)_2$ C15-Laves phase are no longer present. This further indicate that active dissolution of $Cr(VNb)_2$ C15-Laves phase actually occurred when exposed to acidic solution. The formed VO_2 is not sufficient to protect the CrNbTaVW RHEA from pits and the dissolution of $Cr(VNb)_2$ C15-Laves phase. The XRD pattern of IN718 alloy (Fig. 5f) after potentiodynamic polarization showed that no new peaks were formed, signifying that limited or no oxides were deposited on the IN718 alloy surface. Hence, the highly corroded surface and pits observed in the IN718 alloy when exposed to an acidic solution.

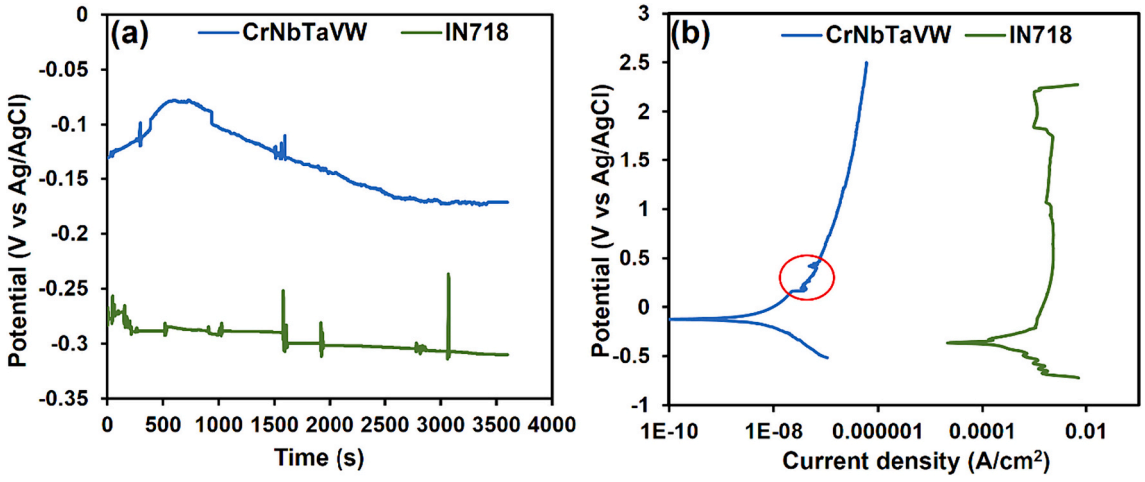


Fig. 4. OCP and potentiodynamic polarization curves for CrNbTaVW RHEA and IN718 alloy in 1 M H_2SO_4 solution: (a) OCP curves of CrNbTaVW RHEA and IN718 alloy in 1 M H_2SO_4. (b) Potentiodynamic polarization curves of CrNbTaVW RHEA and IN718 alloy in 1 M H_2SO_4.

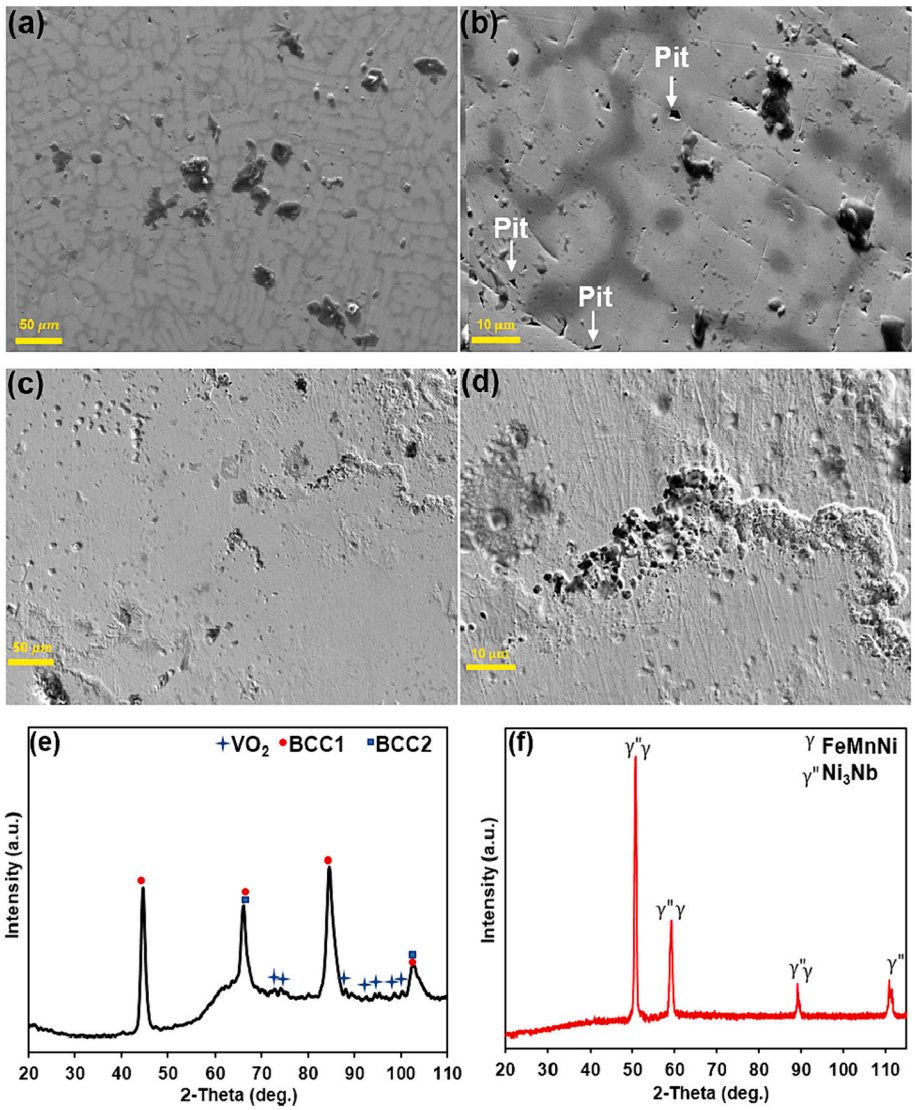


Fig. 5. Surface morphology of the CrNbTaVW RHEA showing the corrosion products and pits after exposure in 1 M H_2SO_4 (a-b); Surface morphology of the IN718 alloy corroded surface and pits after exposure in 1 M H_2SO_4 (c-d); Phase analysis of corrosion products present in the CrNbTaVW RHEA (e); Phase analysis of corrosion products present in the IN718 alloy (f).

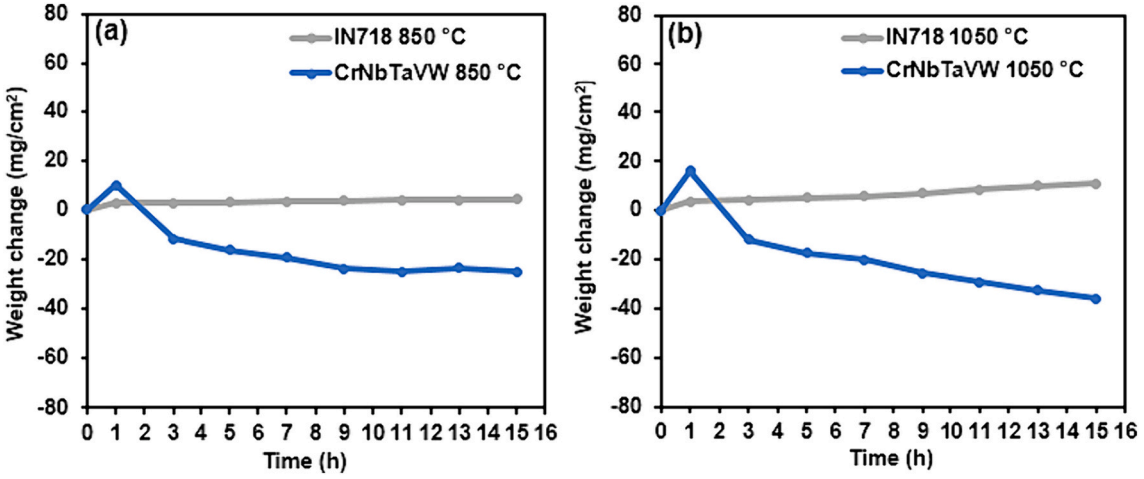


Fig. 6. Cyclic oxidation curve of CrNbTaVW RHEA and IN718 alloy at 850 °C (a); Cyclic oxidation oxidation curve of CrNbTaVW RHEA and IN718 alloy at 1050 °C (b).

4. Oxidation analysis of CrNbTaVW and IN718

4.1. Cyclic oxidation behavior of CrNbTaVW and IN718

The mass gain curves of the CrNbTaVW and IN718 at 850 °C and 1050 °C after 15 hours are shown in Fig. 6. At 850 °C and 1050 °C (Fig. 6a and b), the CrNbTaVW RHEA shows a mass gain at the initial stages due to the alloys reaction with oxygen that facilitated the fast growth of the oxide scale [61]. After 3 hours of oxidation at both temperatures, CrNbTaVW RHEA exhibited rapid mass loss which can be attributed to spallation. At 850 °C (9–15 hours), the mass curve is stationary because the oxide scale gets thicker, thereby protecting the surface of the CrNbTaVW RHEA from direct contact with oxygen. Hence, a decrease in mass loss. However, at 1050 °C (9–15 hours), a continuous mass loss was observed for CrNbTaVW RHEA. The IN718 alloy exhibited an almost stationary trend throughout the oxidation test (Fig. 6a and b). Therefore, the IN718 alloy has a lower mass gain of 4.41 mg/cm^2 and 10.84 mg/cm^2 over the entire 15 hours of oxidation at 850 °C and 1050 °C. Unlike the CrNbTaVW RHEA which exhibited a high mass loss of −25.17 mg/cm^2 and − 35.91 mg/cm^2 at 850 °C and 1050 °C (Fig. 6a and b). The IN718 alloy has a better oxidation resistance than the CrNbTaVW RHEA over the entire 15 hours of oxidation.

4.2. Phase analysis and surface morphologies of oxidized CrNbTaVW and IN718

The XRD patterns of the oxidized CrNbTaVW and IN718 samples at 850 °C and 1050 °C are shown in Fig. 7. The identified oxides of CrNbTaVW RHEA at 850 °C are composed of VO_2, V_2O_3, WO_3, Cr_2O_3, $CrVO_3$, Cr_2WO_6, and $Nb_2O_5WO_3$ (Fig. 7a). At 1050 °C, identified oxides are VO_2, V_2O_3, WO_3, Cr_2O_3, Cr_2WO_6, $CrVO_3$, $Nb_2O_5WO_3$, and $CrTaO_4$ (Fig. 7b). The identified oxides of IN718 at 850 °C were composed of MnO, Ni_2Ti_4O, Al_2O_3, MnO_2, Fe_2O_3, Fe_3O_4, SiO_2, and TiO_2 (Fig. 7c). At 1050 °C, identified oxides are MnO, Fe_3O_4, Mn_2O_3, MnO_2, Fe_2MnO_4, and $NiMn_2O_4$ (Fig. 7d).

The SEM images of the surface oxides of CrNbTaVW RHEA at 850 °C and 1050 °C after 15 hours are shown in Fig. 8. At 850 °C, the surface scale layer is spalled with cracks (15.5 ± 2.14 μm), pores (6.1 ± 0.39 μm), and voids (12.7 ± 0.39 μm) (Fig. 8a). The Cr-rich spalled oxides are also found on the surface (Fig. 8a and Supplementary Fig. 5). Higher magnification of the surface morphology at 850 °C reveals granular-shaped (0.68 ± 0.04 μm) and rod-shaped (1.24 ± 0.11 μm) oxides that were dispersed all over the surface (Fig. 8b). The observed rod-shaped and granular-shaped oxides have been observed in some RHEAs such as CrMoNbTaV [43], NbTiZrV [44], and CrMoNbTaW [62]. The EDS compositions at 850 °C showed that the granular-shaped oxides are rich in Cr, while rod-shaped oxides are NbTaW-rich (Supplementary Fig. 5). Fig. 8(c) shows that the surface morphology of CrNbTaVW RHEA at 1050 °C is spalled with voids (18 ± 1.09 μm). Higher magnification of the surface oxides also contains granular-shaped (0.66 ± 0.03 μm) and rod-shaped (2.73 ± 0.21 μm) that were dispersed all over the alloy surface (Fig. 8d). However, the size of rod-shaped oxides is slightly larger than that observed at 850 °C. Therefore, high temperatures have a major impact on the growth and nucleation of oxides. The EDS compositions at 1050 °C showed that the granular-shaped oxides are rich in Cr, while rod-shaped oxides are rich in Nb/Ta/W (Supplementary Fig. 6).

The SEM images of the surface oxides of IN718 at 850 °C and 1050 °C after 15 hours are shown in Fig. 9. The surface oxide layer of the IN718 at 850 °C showed a compact structure but no cracks, pores, or voids (Fig. 9a). Higher magnification of the top surface oxides of IN718 revealed block-shaped (0.45 ± 0.04 μm), rod-shaped (0.39 ± 0.03 μm),

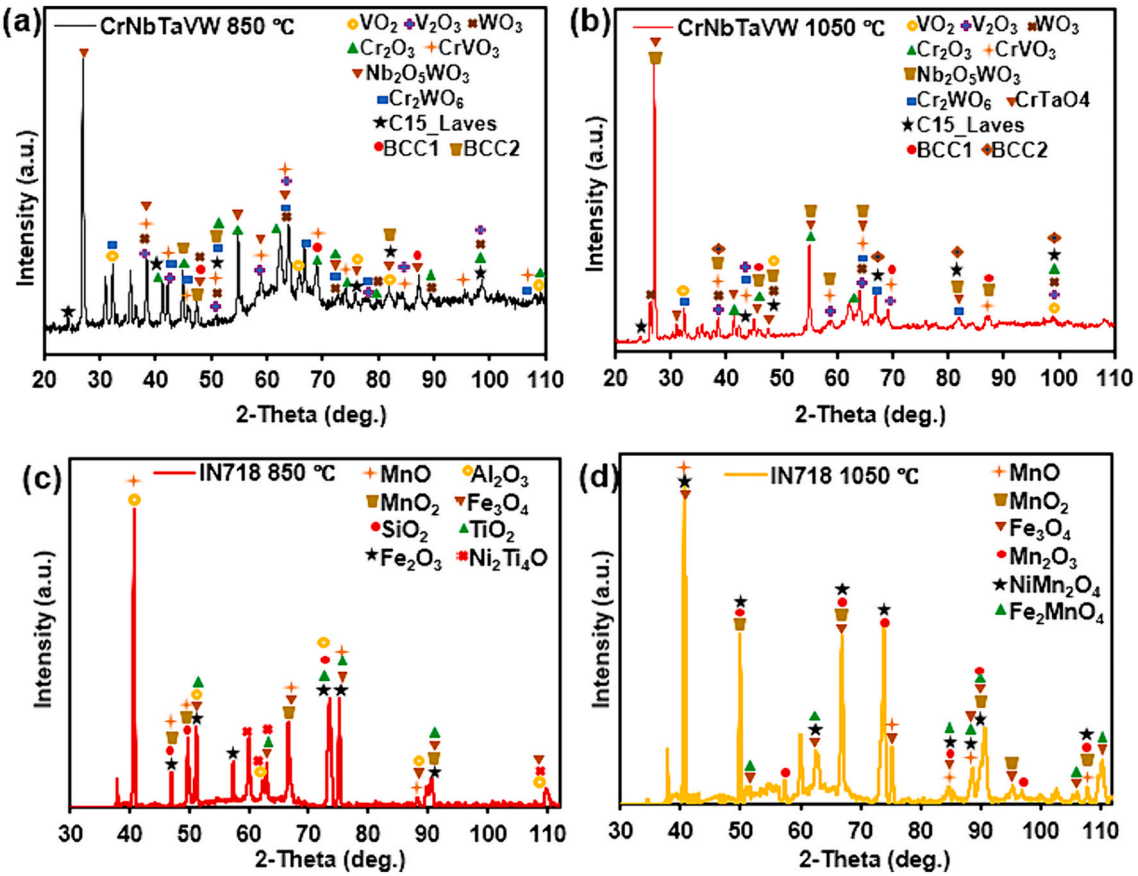


Fig. 7. Phase analysis of identified oxides in CrNbTaVW at 850 °C (a) and 1050 °C (b); Phase analysis of identified oxides in IN718 at 850 °C (c) and 1050 °C (d).

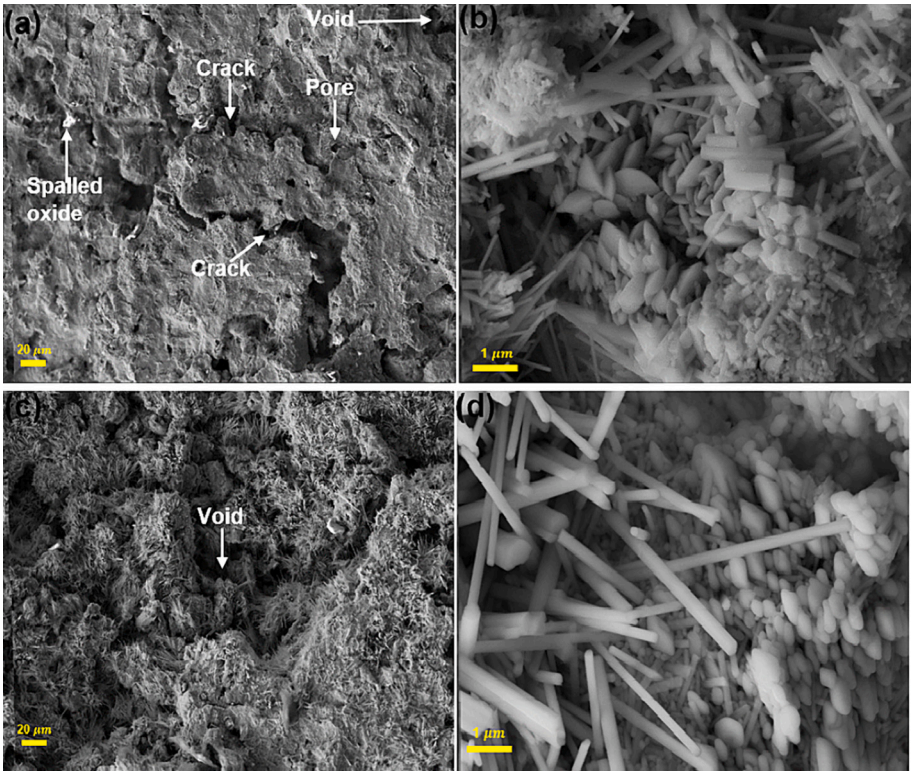


Fig. 8. Surface morphology of the CrNbTaVW RHEA showing voids, cracks, pores, and spalled oxides at 850 °C after 15 hours (a); Higher magnification of the CrNbTaVW RHEA surface morphology showing granular and rod-shaped oxides at 850 °C after 15 hours (b); Surface morphology of the CrNbTaVW RHEA showing voids and spalled oxides at 1050 °C after 15 hours (c); Higher magnification of the CrNbTaVW RHEA surface morphology showing granular and rod-shaped oxides at 1050 °C after 15 hours.

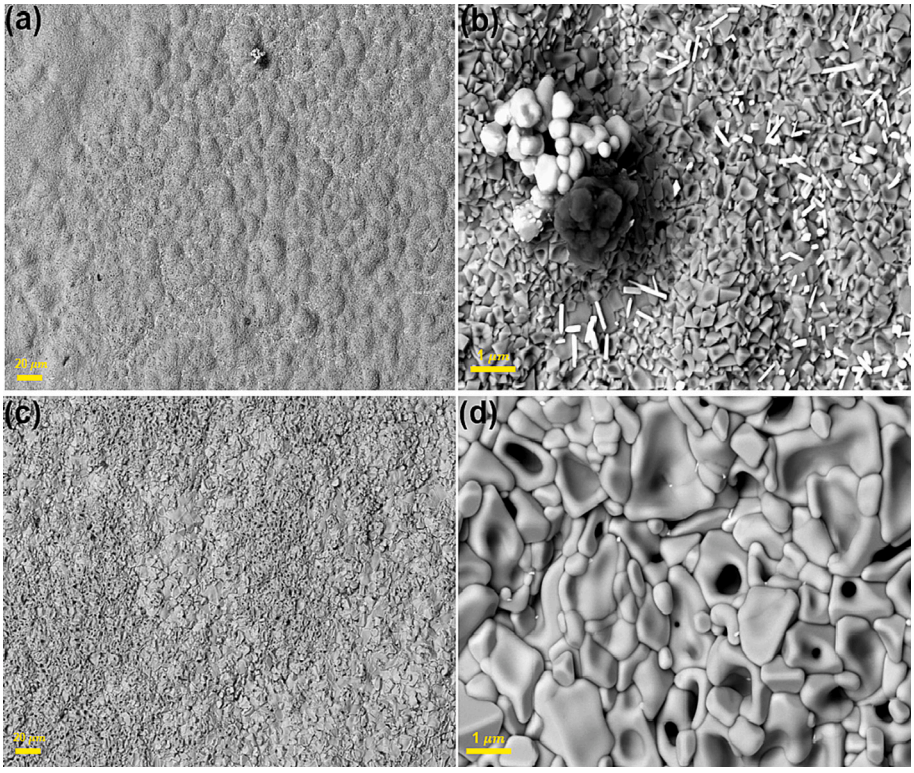


Fig. 9. Surface morphology of the IN718 alloy showing a compact structure at 850 °C after 15 hours (a); Higher magnification of IN718 alloy surface morphology showing block-like, rod-like, round, and cloudy shaped oxides at 850 °C after 15 hours (b); Surface morphology of the IN718 alloy showing a compact and refined structure at 1050 °C after 15 hours (c); Higher magnification of IN718 alloy surface morphology showing globular and block-like oxides at 1050 °C after 15 hours.

round-shaped (0.53 ± 0.05 μm) and cloudy-shaped oxides (0.50 ± 0.04 μm) (Fig. 9b). The EDS compositions at 850 °C showed that the block shaped oxides are Fe-rich, rod-shaped oxides are FeMnNi-rich, round shaped oxides (white) are TiFeSi-rich, and cloudy shaped oxides (dark) are AlSi-rich (Supplementary Fig. 7). At 1050 °C, IN718 surface oxide layer comprises a more refined structure that is free of cracks, pores, or voids (Fig. 9c). Higher magnification of the surface oxides revealed globular (0.35 ± 0.02 μm) and block-shaped oxide structures (1.11 ± 0.12 μm) (Fig. 9d). The EDS compositions at 1050 °C showed that the globular and block-like oxide structures are majorly enriched in Fe (Supplementary Fig. 8).

4.3. Cross sectional morphologies of oxidized CrNbTaVW and IN718

SEM-BSD images of the cross-section morphologies of CrNbTaVW RHEA and IN718 alloy after oxidation at 850 °C and 1050 °C for 15 hours are shown in Fig. 10. At 850 °C, a 260 ± 7.8 μm thick oxidized layer with grey contrast and a 29 ± 5.5 μm thick internal oxidation zone was observed for CrNbTaVW RHEA (Fig. 10a). The thick oxide layer contains tiny cracks that are connected to voids that are 31 ± 1.7 μm thick. It is believed that the cracks grow to form the observed voids. The EDS compositions at 850 °C/15 hours showed mostly WNbTa-rich oxides for both the thick oxide layer and internal oxidation zone (Supplementary Fig. 9). At 1050 °C, a 603 ± 9.1 μm thick oxidized layer with grey contrast was observed for CrNbTaVW RHEA (Fig. 10b). Cracks and voids of 8.5 ± 0.81 μm and 35 ± 2.71 μm was also observed in the thick oxide layer (Fig. 10b). The EDS compositions of the thick oxide layer at 1050 °C/15 hours showed mainly WNbTaCr-rich oxides (Supplementary Fig. 10). As the oxidation temperature increased from 850 °C to 1050 °C, the thickness of the oxide layer increased from 260 μm to 603 μm. Oxide layer tends to serve as a reliable diffusion barrier that effectively isolates the substrate from oxygen and therefore the oxidation rate of the metallic substrate is decreased [3]. The oxide layers are porous with voids and cracks at 850 °C and 1050 °C that limit the formation of a reliable diffusion barrier. The voids and cracks allow the ingress of oxygen into the metallic substrate and therefore the oxidation rate of the metallic substrate is increased.

At 850 °C and 1050 °C, the IN718 alloy displays two layers, which are defined as the outer oxide layer and the internal oxide layer. At 850 °C, a 38.6 ± 1.1 μm thick outer oxide layer and 46.1 ± 1.4 μm thick internal oxide layer was observed (Fig. 10c). The EDS compositions of the outer oxide layer at 850 °C/15 hours showed mostly Fe-rich oxide, while internal oxide layer comprise of mostly FeNi-rich oxides (Supplementary Fig. 11). At 1050 °C, the outer oxide layer has a thickness of 15.34 ± 0.6 μm, while the internal oxide layer has a thickness of 66.8 ± 3.3 μm (Fig. 10d). EDS compositions of the outer oxide layer and internal oxide layer at 1050 °C/15 hours comprise mostly FeNi-rich oxides (Supplementary Fig. 11). It was observed that the internal oxide layer has higher thickness than the outer oxide layer at 850 °C and 1050 °C. The IN718 oxidation rate is lower at both temperatures because the outer and internal oxide layers serve as diffusion barriers.

5. Discussion

5.1. CrNbTaVW phase prediction

The physical properties of elements in the CrNbTaVW RHEA and enthalpy of mixing for the selected alloy binary subsystem are shown in Table 5. In Table 5, Ta possesses the largest atomic radius and smallest electronegativity, while Cr possesses the smallest atomic radius. There could have been atomic distortion during the mixing of elements due to the large atomic size difference between the elements, leading to an increase in lattice strain. The large atomic size difference between so many components would considerably impact the formation of solid solutions in multi-component alloys. The empirical phase parameters are calculated and shown in Table 6.

In Table 5, CrNb (−7), CrTa (−7), NbW (−8), TaW (−7), CrV (−2) have a significant negative enthalpy of mixing, indicating the formation

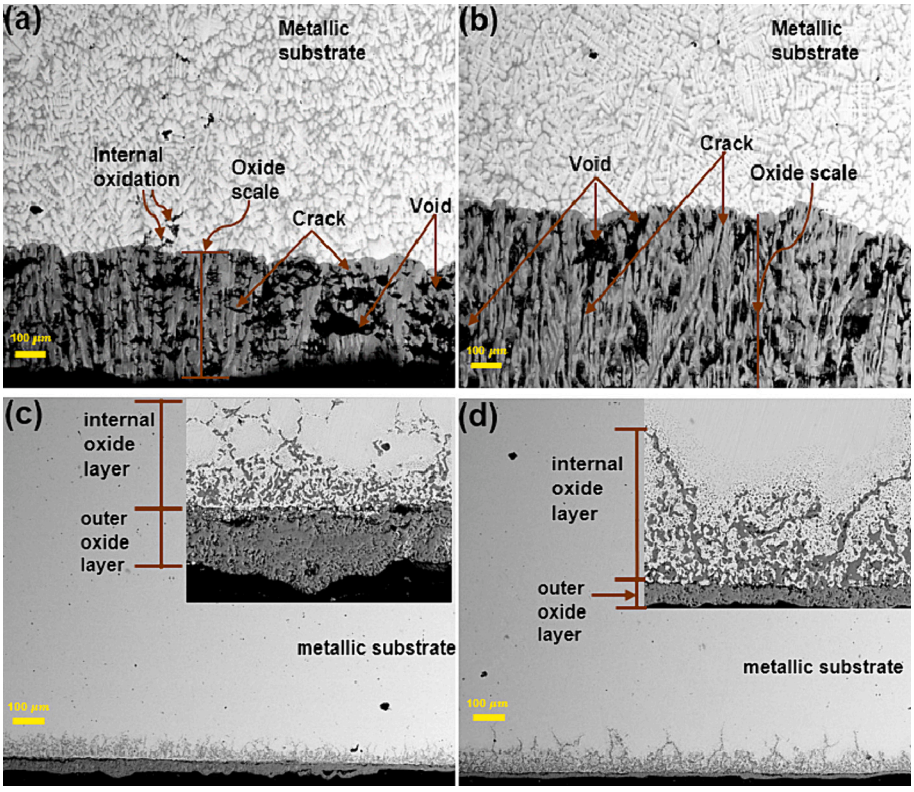


Fig. 10. Cross-sectional morphology of CrNbTaVW RHEA at 850 °C and 1050 °C after 15 hours (a-b); Cross-sectional morphology of IN718 at 850 °C and 1050 °C after 15 hours (c-d).

Table 5
Physical properties of elements in the CrNbTaVW RHEA and their binary enthalpy of mixing [5,63].

Elements	Cr	Nb	Ta	V	W
Atomic radius ($\AA$)	1.27	1.43	1.46	1.32	1.39
Density (Kg/m^3)	7.19	8.57	16.4	6.0	19.3
Melting temperature ($^\circ$C)	1907	2477	3017	1910	3414
Valence electron	6	5	5	5	6
Electronegativity(χ)	1.66	1.60	1.50	1.63	2.36
Hardness (HV)	108	134	89	64	349

Binary enthalpy of mixing[1]										
i - j	CrNb	CrTa	CrV	CrW	NbTa	NbV	NbW	TaV	TaW	VW
ΔH_{ijmix}	−7	−7	−2	1	0	−1	−8	−1	−7	−1

[1] rsc.org

Table 6
Calculated empirical phase parameters.

Solid solution parameters	References	Range of parameters	Calculated values for the CrNbTaVW RHEA
$VEC = \sum_{i=1}^{n} C_i(VEC)i$	[64,65]	VEC < 6.87 = BCC VEC ≥ 8 = FCC 6.87 ≤ VEC < 8 = BCC + FCC	5.4
$\Delta H_{mix} = \sum_{i=1, i\neq j}^{n} 4\Delta Hij^{mix} C_i\, C_j$	[65,66]	−15 kJ/mol ≤ ΔH_{mix} ≤ 5 kJ/mol	−5.03 kJ/mol
$\Delta S_{mix} = -R\sum_{i=1}^{n} C_i lnC_i$	[65,66]	High value of entropy of mix is important in stabilizing the solid solution phases	13.38 J/K mol
$\delta = \sqrt{\sum_{i=1}^{n} C_i(1 - r_i/\bar{r})^2}$	[65,67,68]	$\delta \leq 6.6\%$ = BCC $\delta \geq 6.6\%$ = FCC and Laves	5.09%
$\Omega = \frac{T_m \Delta S_{mix}}{\Delta H_{mix}}, T_m = \sum_{i=1}^{n} C_i(T_m)i$	[66]	Ω ≥ 1.1	6.77
$\Delta\chi = \sqrt{\sum_{i=1}^{n} C_i(X_i - \bar{X})^2}$	[69]	$\Delta\bar{X}$ must be small to form a solid solution	0.31
$\Lambda = \Delta S_{mix}/\delta^2$	[70]	Λ > 0.96 = single phase. 0.24 < Λ <0.96 = two-phase	0.52

of intermetallic compound. A good mutual solubility is revealed in the NbTa (0), NbV (−1), TaV (−1) and VW (−1) binary systems, indicating the formation of a solid-solution phase. The CrW is the only positive binary enthalpy of mixing among each pair of the constituent elements in the CrNbTaVW RHEA that specifies phase separation. According to [71], segregation phenomenon can be described based on positive binary enthalpy of mixing among each pair of the constituent elements. The more positive ΔH_{mix} means the less miscibility of the different elements in the liquid alloy, which leads to separation of phases or segregation of different elements in the alloy [66]. As seen in Fig. 1(a), a Laves phase was formed which is in agreement with the binary enthalpy (CrV (−2)), since it has a higher negative enthalpy among the binary enthalpies. The presence of Laves phases can significantly influence the physical and mechanical properties of HEAs [11,72-74] Senkov, Senkova, Woodward, et al., 2013; Xiang et al., 2020). The main factors affecting the Laves phase structure are the atomic size factor and the electron concentration factor [73]. The Laves phase formed due to the difference in atomic size and electronegativity between Cr and the other four elements making up the CrNbTaVW RHEA. The binary enthalpies alone cannot predict the phases and crystal structure. The calculated empirical parameters for the CrNbTaVW RHEA in Table 6 compared with three proposed criteria [65,66,75] were used to further predict the phases and crystal structure.

The first criterion states that the disordered solid solution phase forms when Ω >1.1 and δ < 6.6% [66]. The CrNbTaVW RHEA has Ω = 6.77 which is >1.1, while δ (5.09) was <6.6%. This means that the disordered solid solution BCC phase will occur. Although Ω was >1.1, it cannot differentiate between single and multi-phase solid solutions. To fill the void, Λ in Table 6 was proposed and the CrNbTaVW RHEA has a lesser geometrical parameter of 0.52, which indicates a multiphase solid solution structure. The second criterion states that FCC and BCC crystal structures would be stable, if VEC ≥ 8 and VEC ≤ 6.87 respectively [65]. The CrNbTaVW RHEA has a VEC of 5.4 which is <6.87. A stable BCC crystal structure formed. The third criterion states that Laves phase forms when $\Delta\chi > 7\%$ and $\delta > 5\%$ in HEAs [75]. In the CrNbTaVW RHEA, $\Delta\chi = 0.31$ and is lower than 7%. However, the atomic size mismatch parameter for CrNbTaVW is 5.09%, which is higher than 5%. Hence, the Laves phase is expected to occur in the CrNbTaVW RHEA. The first two criteria successfully predicted a multi-phase solid solutions phase, whereas in criterion three, only the lattice distortion parameter predicted the Laves phase. This provides a reasonable agreement with the experimental results as evidenced in Fig. 1. The phase separation agrees with Λ parameter by Singh and Subramaniam [70], which predicted the formation of multi-phase solid solutions in CrNbTaVW RHEA.

5.2. Corrosion resistance of CrNbTaVW RHEA in 3.5 wt% NaCl and 1 M H_2SO_4 solution

Passivation is a characteristic of HEAs, arising due to the addition of passivating promoting elements such as Cr and Ti. The passivating promoting element may influence the alloy structure and passive film composition, giving rise to different electrochemical responses depending on the alloying type and content [76]. The SEM images of the CrNbTaVW RHEA in chloride solution showed few pits, while in acidic solution, more pits and selective dissolution of $Cr(VNb)_2$ Laves took place. HEAs that contain Cr compositions greater than 13 wt% can be associated with enhanced corrosion resistant properties [77]. Despite the high chromium compositions in the RHEA, pits were still found when exposed to NaCl solution. In the H_2SO_4 solution, low Cr composition (10 wt%) was observed in the BCC1, which may have caused the few pits observed in the BCC1 region and none in the BCC2 (Fig. 7b). Regardless of the effects of the aggressive corrosive solutions, the resistance to passive film breakdown is determined by the properties of the passive film including its continuity, formation ability, and film stability [19]. Only VO_2 was formed on the surface of the CrNbTaVW RHEA in both chloride and acidic solutions. The VO_2 layer was able to

prevent phase dissolution and surface corrosion in chloride solution, but not enough protection against localized corrosion (pitting). The microstructure and composition are the two main factors in the corrosion performance of an alloy [77]. Alloy heterogeneities such as inclusions, impurities, and second phases have been reported to be detrimental to the continuity of the overlying passive film of alloys because the oxides formed at these sites or along their edge are often not protective. Thus, the oxide in these areas often acts as the weak spot for breakdown [78,79].

Fig. 11 illustrates the corrosion mechanism of the CrNbTaVW when exposed to 3.5 wt% NaCl and 1 M H_2SO_4 solutions. At the beginning of corrosion in NaCl environment (Fig. 11a), Cl^- is adsorbed on the passive film, which makes some metal cations in the passive film dissolve into the solution. The CrNbTaVW RHEA comprise multiphases of BCC1, BCC2, and $Cr(VNb)_2$ Laves, Cl^- will be preferentially adsorbed in these phases and detrimental to the passive film continuity. It was observed that pitting occurred mostly in BCC1 and regions between the BCC1 and BCC2 phases (Fig. 11b). The pits can be initiated by the elemental segregation of the elements that comprises the two phases. If there is a significant potential difference between the two phases, galvanic coupling can result in localized corrosion (pits) [80,81]. The passive film properties made BCC1 phase the anode and BCC2 phase the cathode, the passive film eventually weakened resulting in the pitting of BCC1 phase under the combined effect of galvanic coupling and Cl^- (Fig. 11b).

In an acidic solution, fluctuations were observed in passive film indicating dissolution of the protective film (Fig. 4a). The dissolution of the protective film on the alloy can be attributed to the SO_4^{2-} ions in the solution (Fig. 11c). As the CrNbTaVW RHEA is immersed in the 1 M H_2SO_4, the anode and cathode areas are electrically connected and constitute the corrosion cell, leading to the existence of electric potential. Pits initiate mainly on the BCC1 phase and the boundaries of the BCC1 and BCC2 phases (Fig. 11d). The observed pit in the BCC1 phase could be attributed to combined effect of SO_4^{2-} ions and galvanic coupling of the BCC1 phase (anode) and BCC2 phase (cathode) (Fig. 11d). The $Cr(VNb)_2$ Laves phase was formed on top of the BCC2 phase and boundaries between the two phases are often weak zones and preferential to initiate corrosion. The potential difference between dual phases brings about a strong driving force for phase dissolution [80,82]. As a result of coupling effects between the $Cr(VNb)_2$ Laves phase (anode) and BCC2 phase (cathode), the $Cr(VNb)_2$ Laves was eventually dissolved (Fig. 11d). Despite the pits observed in the BCC1 phase and the dissolution of $Cr(VNb)_2$ Laves, the CrNbTaVW RHEA still has a high corrosion resistance in both the chloride and acidic solutions.

5.3. Oxidation mechanism

At 850 °C and 1050 °C, simple oxides of VO_2, V_2O_3, WO_3, and Cr_2O_3 form on the oxidized CrNbTaVW at the initial stages. The stability and formation of the simple oxides at 850 °C using the Gibbs free energy ($\triangle G$) values follow the following order: V_2O_3 (−639) > Cr_2O_3 (−555) > VO_2 (−521) > WO_3 (−384) [31,83]. At 1050 °C, the stability and the formation of favorable oxides follows the order: V_2O_3 (−602) > Cr_2O_3 (−527) > VO_2 (−467) > WO_3 (−346) [31,83]. The WO_3 has the largest $\triangle G$ values which makes it the least stable simple oxide formed on the surface of the CrNbTaVW RHEA at 850 °C and 1050 °C. At increasing oxidation time, the simple oxides will continuously react and combine into complex oxides, as seen in Eqs. (1)–(6).

$$CrO\ (s) + VO_2\ (s) = CrVO3\ (s) \quad (1)$$

$$Cr_2O_3\ (s) + WO_3(s) = Cr_2WO_6\ (s) \quad (2)$$

$$8WO_3(s) + 4Ta_2O_5(s) = Ta_8W_8O_{44}\ (s) \quad (3)$$

$$Nb_2O_5\ (s) + WO_3(s) = Nb_2O_5.WO_3\ (s) \quad (4)$$

$$1/2Cr_2O_3\ (s) + 1/2Ta_2O_5\ (s) = CrTaO_4\ (s) \quad (5)$$

$$1/2Cr_2O_3\ (s) + 1/2Nb_2O_5\ (s) = CrNbO_4\ (s) \quad (6)$$

The high diffusion coefficient of Cr enables the synthesis of VO_2, Ta_2O_5, and Nb_2O_5 into $CrVO_3$, $CrTaO_4$, and Nb_2O_5. Also, Cr_2O_3 react with poor stability WO_3 to synthesize Cr_2WO_6 through the solid–state reaction. Similarly, Ta_2O_5 and Nb_2O_5 reacts with WO_3 to form $Ta_8W_8O_{44}$ and $Nb_2O_5.WO_3$. Complex oxide such as $Ta_8W_9O_{47}$ has been reported to possess low $\triangle G$ (−5400 kJ/mol), leading to a stable oxide layer [84]. In regards to $CrVO_3$ and $Nb_2O_5.WO_3$, it is still unclear whether the oxides would offer oxidation resistance. The addition of V in alloys forms VO_x that volatilizes at high temperatures and prevents the formation of a protective oxide layer [56,68,69]. An oxide layer containing $CrTaO_4$ has been reported to effectively retard oxygen diffusion and provide protection against oxidation at high temperatures [41,43,85]. Similarly, $CrTaO_4$ oxide layer was observed in W containing MoTaTiCr RHEAs that retarded oxygen diffusion and provided great protection against

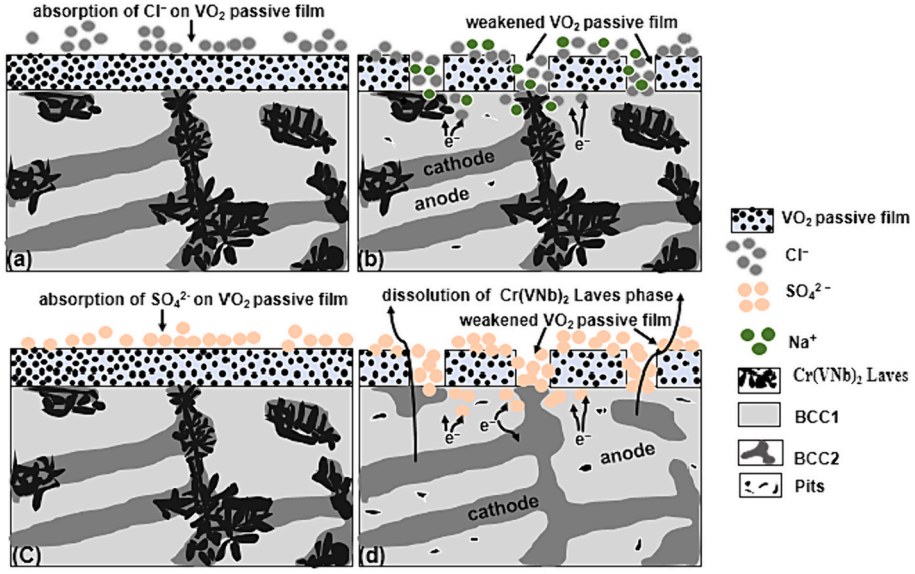


Fig. 11. Schematic diagram of the pits of BCC1 phase in CrNbTaVW RHEA in 3.5 wt% NaCl solution (a-b); Schematic diagram of the pits of BCC1 phase and dissolution of $Cr(VNb)_2$ Laves phase in CrNbTaVW RHEA in 1 Mol H_2SO_4 solution (c-d).

oxidation at 1000 °C [86]. In WCr alloys by Hou et al. [87], oxide scale of Cr_2WO_6 is poor and does not offer protection for further oxidation. However, the Cr_2O_3 scale was sufficient to offer a better protective scale for the WCr alloys. At a particular stage in CrNbTaVW RHEA oxidation at 1050 °C/15 hours, oxides of $CrTaO_4$, $CrNbO_4$, and Cr_2O_3 would have formed a barrier for both inward diffusion of oxygen and outward diffusion. These would have prevented more pores, cracks, and total degradation of the CrNbTaVW RHEA. The oxygen ions diffusion is hindered to some extent by Cr_2O_3 which slowed down the oxidation rate of oxidized CrNbTaVW RHEA.

Small decohesion of the oxide layer was observed for IN718 alloy oxide scale at 850 °C and 1050 °C which might be attributed to the volume change and internal pressures of SiO_2. According to Sheikh et al. [88], formation of MoO_3 and SiO_2 results in a local volume change and internal pressures that lead to decohesion and microcrack formation. Since there are no micro cracks and pores, the observed SiO_2 might not be detrimental to the oxidation resistance of IN718 alloy. The simple oxides such as Al_2O_3 protected the formation and volatilization of Mn_2O_3 in the IN718 at 850 °C and the oxidation rate was further reduced. The Al_2O_3 layer acts as a diffusion barrier against oxygen ingress into the alloy, thereby improving the alloy performance against high-temperature oxidation [89]. The oxide layer containing FeO on the surface is usually loose, porous, and easy to shed, which greatly reduces oxidation resistance [90]. FeO also formed in the IN718 at 1050 °C which might have also contributed to the small decohesion of IN718 alloy oxide scale. Fe_3O_4 observed at 850 °C and 1050 °C further formed a protective continuous layer and lowered the oxidation rate.

The volumetric expansion mismatch generates stresses in the oxides, which accumulate when the oxides grow and later released by cracking, and spallation of oxides from the base alloy [91]. In oxide scales, mechanical stress has two origins: the first is the growth stress, which develops during the oxidation process, and second is the thermal stress which develops due to the change in temperature [91]. The oxide layer of oxidized RHEAs can exfoliate from the metallic substrate during the cooling process from oxidation temperature to room temperature, which is attributed to different coefficients of thermal expansion and specific volume of the oxide and the alloy [92,93]. The growth stress can be quantified by the volume difference between the oxide and the metal forming the oxide and can be expressed by the Pilling-Bedworth ratio (PBR) in Eq. (7) [94].

$$\mathrm{PBR} = \frac{\text{volume per metal ion in oxide}}{\text{volume per metal atom in metal}} \tag{7}$$

The oxide scale is discontinuous and porous if PBR < 1 [24]. For PBR > 2, the internal stress between oxides and matrix is high, and easily leads to the formation of pores, cracks, and spallation [24]. Spallation possibly occurs during the sample cooling due to the large differences between the thermal expansion coefficients of the oxide and the metal [88]. During the cooling stage, the metal substrate contracts more rapidly than the oxide layer, causing compressive in-plane stresses and the creation of shear cracks in the oxide layer [95]. At 850 °C and 1050 °C, cracks, pores, and voids were observed.

Using Eq. (7), the PBR for VO_2, V_2O_3, WO_3, and Cr_2O_3 is 2.17, 1.84, 3.39, and 2.02, respectively. The internal stress between VO_2, WO_3, and Cr_2O_3 and CrNbTaVW substrate is high, which led to the formation of pores and cracks at 850 °C and 1050 °C. In the WMoTaTiCr RHEA, WO_3 exhibited a large PBR that hinders the continuous protective layer [86]. According to Kuang et al. [96], volume expansion ratio of WO_3 would cause a large interface stress that would even tear the adhesive surface oxide scale, providing a channel for oxygen internal diffusion. The growth strain (ε) induces a change in volume that is expressed in Eq. (8) [97].

$$\varepsilon = \sqrt[3]{\mathrm{PBR}} - 1 \tag{8}$$

The ε value was calculated by substituting the PBR values for VO_2, WO_3, and Cr_2O_3 in Eq. (8). The calculated ε value for VO_2, WO_3, and Cr_2O_3 is 0.296, 0.503, and 0.264, respectively. The growth stress (σ_G) can be calculated based on growth strain in Eq. (9) [91].

$$\sigma_G = \varepsilon E_{oxides} \tag{9}$$

Where E_{oxides} is the Young's modulus of VO_2 (140 GPa) [98], WO_3 (300 GPa) [99], and Cr_2O_3 (260 GPa) [91]. By substituting E_{oxides} and ε values into Eq. (9), the σ_G is calculated to be 41.4 GPa, 150.8 GPa, and 68.7 GPa for VO_2, WO_3, and Cr_2O_3, respectively. It can be observed that the σ_G in VO_2 and Cr_2O_3 is less than that of WO_3. It can be assumed that decohesion is only initiated on the oxide scale by VO_2 and Cr_2O_3, while cracks, pores, voids and spalling is initiated by WO_3.

Thermal stress (σ_T) occurred during cooling to room temperature and it was formed due to different thermal expansions between the oxide scales and the CrNbTaVW RHEA. The σ_T can be expressed in Eq. (10) [91].

$$\sigma_T = E_{oxides}\left(\alpha_{alloy} - \alpha_{oxides}\right)\Delta T \tag{10}$$

Where α_{alloy} and α_{oxides} are the thermal expansion coefficients of CrNbTaVW RHEA and the oxides respectively. ΔT is the difference between oxidation temperature and room temperature during cooling. The $\alpha_{CrNbTaVW}$ was calculated to be $10.698 \times 10^{-6}\ K^{-1}$ using the rule of mixture. While α_{oxides} for VO_2, WO_3, and Cr_2O_3 is $2.1 \times 10^{-6}\ K^{-1}$ [98], $8.9 \times 10^{-6}\ K^{-1}$ [100], and $9.6 \times 10^{-6}\ K^{-1}$ [91]. The σ_T is assumed to be generated mainly by VO_2, WO_3, and Cr_2O_3 at 850 °C and 1050 °C. The σ_T generated by VO_2, WO_3, and Cr_2O_3 at 850 °C is estimated to be 0.993 GPa, 0.445 GPa, and 0.199 GPa. At 1050 °C, σ_T generated by VO_2, WO_3, and Cr_2O_3 is 1.234 GPa, 0.553 GPa, and 0.248 GPa. From the results, it can be observed that σ_T is lower than σ_G and the thermal expansion coefficient of the alloy is larger than that of the oxides. Hence, the σ_T in the scale should be compressive, which is the same as growth stress [91]. The failure of protective oxide scales could be due to the mismatch in volume expansion between VO_2, WO_3, and Cr_2O_3 oxides, and CrNbTaVW substrates, which led to the build-up of thermal stress and growth stress.

The summary of the oxidation mechanism of CrNbTaVW RHEA at 850 °C and 1050 °C for 15 hours is shown in Fig. 12. During the initial stage, oxygen dissolves and diffuses internally through the BCC1, BCC2 and $Cr(VNb)_2$ Laves. At higher temperatures, the oxides react with elements that comprise the RHEA and form the simple and complex oxides. The formed oxides at 850 °C and 1050 °C might not be protective due to the mismatch in volume expansion between the oxides and CrNbTaVW substrates. In the oxide scales of CrNbTaVW RHEA, thermal and growth stress was observed. As oxides grows during oxidation, growth stress due to micro-inhomogeneity of oxide species was formed and eventually released via pores, cracks, and voids (Fig. 12a and b). During the cooling to room temperature of CrNbTaVW RHEA, spallation, pores, and voids appear due to thermal stress caused by the different thermal expansion coefficients of the oxides and metallic substrate. The observed pores, cracks, voids, and spallation stresses serves as fast migration channels for oxygen that increases the oxidation rate of the CrNbTaVW RHEA.

6. Conclusions

The microstructure, hardness, corrosion, and oxidation behavior of CrNbTaVW RHEA have been investigated. The results were compared to commercial grade IN718 nickel-based superalloy. The following conclusions are drawn from the study:

- The as-cast CrNbTaVW RHEA exhibited a dendritic microstructure that segregated into BCC1, BCC2, and $Cr(VNb)_2$ Laves. The empirical calculations, XRD, and SEM accurately predicted the phases in the CrNbTaVW RHEA.
- The hardness test result of CrNbTaVW RHEA after ten indentations found the hardness value to be 688 ± 21 HV, which is higher than

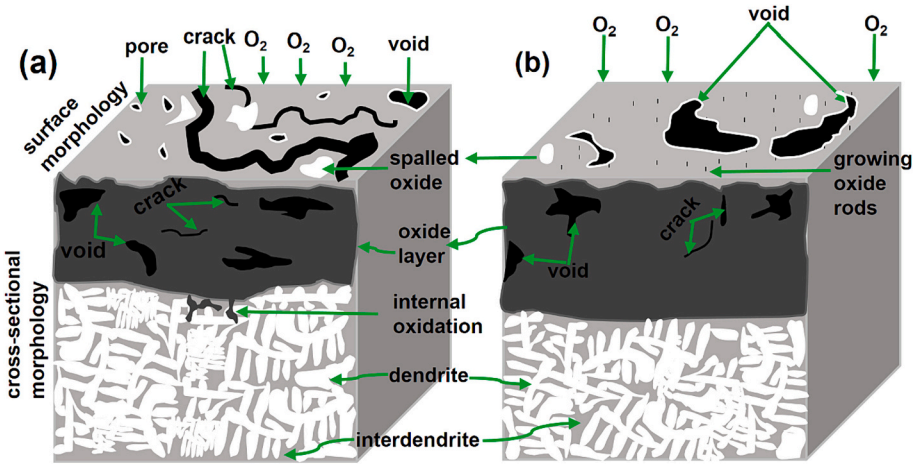


Fig. 12. Schematic diagram of the oxidation mechanism of CrNbTaVW at 850 °C and 1050 °C after 15 hours (a-b).

IN718 (301 ± 14 HV). The high hardness of CrNbTaVW RHEA is attributed to Laves phase solid solution strengthening and grain refinement.

- Fluctuations in OCP were observed for CrNbTaVW RHEA in 1 M H_2SO_4 solutions and IN718 alloy in both 3.5 wt% NaCl and 1 M H_2SO_4 solutions.
- The CrNbTaVW RHEA has a lower corrosion rate of 0.000097 mm/yr in 3.5 wt% NaCl solution than the IN718 alloy (0.054 mm/yr). In acidic solution, CrNbTaVW RHEA has a low corrosion rate of 0.00013 mm/yr in 1 M H_2SO_4 solution than the IN718 alloy (1.12 mm/yr). Therefore, it can be concluded that CrNbTaVW RHEA has superior corrosion resistance in 3.5 wt% NaCl and 1 M H_2SO_4 solution in comparison with commercial grade IN718.
- In chloride solution, BCC1 is more susceptible to pitting corrosion. In acidic solution, BCC1 is more susceptible to pitting corrosion, while the $Cr(VNb)_2$ Laves phase is more susceptible to selective dissolution.
- The IN718 alloy has a lower mass gain of 4.41 mg/cm^2 and 10.84 mg/cm^2 at 850 °C/15 hours and 1050 °C/15 hours. The CrNbTaVW RHEA exhibited a mass loss of −25.17 mg/cm^2 and − 35.91 mg/cm^2 at 850 °C/15 hours and 1050 °C/15 hours. In general, the IN718 alloy has a superior oxidation resistance than the CrNbTaVW RHEA.
- Thermal stress and growth stress contributed to pores, voids, cracks, and spallation observed in the CrNbTaVW RHEA at 850 °C and 1050 °C after 15 hours. The pores, cracks, and voids allow ingress of oxygen to the metallic substrate and increased the oxidation rate.

CRediT authorship contribution statement

Olufemi Sylvester Bamisaye: Writing – original draft, Methodology, Investigation, Formal analysis, Conceptualization. **Nthabiseng Maledi:** Writing – review & editing, Validation, Supervision, Resources, Methodology, Conceptualization. **Josias Van der Merwe:** Supervision, Resources, Methodology, Conceptualization. **Michael Oluwatosin Bodunrin:** Writing – review & editing, Validation, Supervision, Resources, Methodology, Conceptualization.

Declaration of competing interest

The authors declare that there is no conflict of interest to this work.

Data availability

Data will be made available on request.

Appendix A. Supplementary data

Supplementary data to this article can be found online at https://doi.org/10.1016/j.ijrmhm.2024.106661.

References

[1] B. Cantor, I.T.H. Chang, P. Knight, A.J.B. Vincent, Microstructural development in equiatomic multicomponent alloys, Mater. Sci. Eng. A 375–377 (2004) 213–218, https://doi.org/10.1016/j.msea.2003.10.257.
[2] J. Yeh, S. Chen, S. Lin, J. Gan, T. Chin, T. Shun, C. Tsau, C. Shou-Yi, Nanostructured high-entropy alloys with multiple principal elements: novel alloy design concepts and outcomes, Adv. Eng. Mater. 6 (2004) 299–303, https://doi.org/10.1002/adem.200300567.
[3] B. Gorr, F. Müller, M. Azim, H.J. Christ, T. Müller, H. Chen, A. Kauffmann, M. Heilmaier, High-temperature oxidation behavior of refractory high-entropy alloys: effect of alloy composition, Oxid. Met. 88 (2017) 339–349, https://doi.org/10.1007/s11085-016-9696-y.
[4] J.W. Yeh, S.K. Chen, S.J. Lin, J.Y. Gan, T.S. Chin, T.T. Shun, C.H. Tsau, S. Y. Chang, Nanostructured high-entropy alloys with multiple principal elements: novel alloy design concepts and outcomes, Adv. Eng. Mater. 6 (2004) 299–303, https://doi.org/10.1002/adem.200300567.
[5] O.N. Senkov, G.B. Wilks, D.B. Miracle, C.P. Chuang, P.K. Liaw, Refractory high-entropy alloys, Intermetallics 18 (2010) 1758–1765, https://doi.org/10.1016/j.intermet.2010.05.014.
[6] D.B. Miracle, O.N. Senkov, A critical review of high entropy alloys and related concepts, Acta Mater. 122 (2017) 448–511, https://doi.org/10.1016/j.actamat.2016.08.081.
[7] S. Nam, Y. Song, M. Son, et al., High-temperature mechanical and thermochemical properties of NbMoTaW refractory high-entropy alloy coatings produced via Nano particle deposition system (NPDS), Int. J. Refract. Met. Hard Mater. 99 (2021) 105594, https://doi.org/10.1016/j.ijrmhm.2021.105594.
[8] J. Liu, R.J. Scales, B.S. Li, et al., Controlling microstructure and mechanical properties of Ti-V-Cr-Nb-ta refractory high entropy alloys through heat treatments, J. Alloys Compd. 932 (2023) 1–7, https://doi.org/10.1016/j.jallcom.2022.167651.
[9] C. Duan, M. Reiberg, P. Kutlesa, et al., Strain-hardening properties of the high-entropy alloy MoNbTaTiVZr processed by high-pressure torsion, Contin. Mech. Thermodyn. 34 (2022) 475–489, https://doi.org/10.1007/s00161-021-01065-5.
[10] A. Poulia, E. Georgatis, A. Lekatou, et al., Microstructure and wear behavior of a refractory high entropy alloy, Int. J. Refract. Met. Hard Mater. 57 (2016) 50–63, https://doi.org/10.1016/j.ijrmhm.2016.02.006.
[11] F.G. Coury, T. Butler, K. Chaput, et al., Phase equilibria, mechanical properties and design of quaternary refractory high entropy alloys, Mater. Des. 155 (2018) 244–256, https://doi.org/10.1016/j.matdes.2018.06.003.
[12] L. Fang, J. Wang, X. Li, et al., Effect of Cr content on microstructure characteristics and mechanical properties of $ZrNbTaHf0.2Cr_x$ refractory high entropy alloy, J. Alloys Compd. 924 (2022), https://doi.org/10.1016/j.jallcom.2022.166593.
[13] O.N. Senkov, S.V. Senkova, D.B. Miracle, et al., Mechanical properties of low-density, refractory multi-principal element alloys of the Cr-Nb-Ti-V-Zr system, Mater. Sci. Eng. A 565 (2013) 51–62, https://doi.org/10.1016/j.msea.2012.12.018.
[14] C. Xiang, Z. Ming, Z. Hua, et al., Microstructure, mechanical properties, and corrosion behavior of MoNbFeCrV, MoNbFeCrTi, and MoNbFeVTi high-entropy alloys, Acta Metall. Sin. 32 (2019) 1053–1064, https://doi.org/10.1007/s40195-019-00935-x.

[15] D.H. Xia, C.M. Deng, D. Macdonald, et al., Electrochemical measurements used for assessment of corrosion and protection of metallic materials in the field: a critical review, J. Mater. Sci. Technol. 112 (2022) 151–183, https://doi.org/10.1016/j.jmst.2021.11.004.

[16] Y. Shi, B. Yang, P.K. Liaw, Corrosion-resistant high-entropy alloys: a review, Metals 7 (2017) 1–18, https://doi.org/10.3390/met7020043.

[17] D. Yan, K. Song, Microstructures, mechanical properties, and corrosion behaviors of refractory high-entropy alloys, J. Mater. Eng. Perform. 29 (2020) 399–409, https://doi.org/10.1007/s11665-019-04540-y.

[18] Q. Zhou, S. Sheikh, P. Ou, et al., Corrosion behavior of $Hf_{0.5}Nb_{0.5}Ta_{0.5}Ti_{1.5}Zr$ refractory high-entropy in aqueous chloride solutions, Electrochem. Commun. 98 (2019) 63–68, https://doi.org/10.1016/j.elecom.2018.11.009.

[19] T. Li, O.J. Swanson, G.S. Frankel, et al., Localized corrosion behavior of a single-phase non-equimolar high entropy alloy, Electrochim. Acta 306 (2019) 71–84, https://doi.org/10.1016/j.electacta.2019.03.104.

[20] Q. Zhou, S. Sheikh, P. Ou, et al., Corrosion behavior of $Hf_{0.5}Nb_{0.5}Ta_{0.5}Ti_{1.5}Zr$ refractory high-entropy in aqueous chloride solutions, Electrochem. Commun. 98 (2019) 63–68, https://doi.org/10.1016/j.elecom.2018.11.009.

[21] Y. Gao, K. Chong, L. Qiao, et al., Synthesis and corrosion behavior of $Mo_{15}Nb_{20}Ta_{10}Ti_{35}V_{20}$ refractory high entropy alloy, Mater. Des. 228 (2023) 1–15, https://doi.org/10.1016/j.matdes.2023.111820.

[22] M. Li, Q. Chen, X. Cui, et al., Evaluation of corrosion resistance of the single-phase light refractory high entropy alloy TiCrVNb0.5Al0.5 in chloride environment, J. Alloys Compd. 857 (2021) 1–10, https://doi.org/10.1016/j.jallcom.2020.158278.

[23] D. Bi, Y. Chang, H. Luo, et al., Corrosion behavior and passive film characteristics of $AlNbTiZrSi_x$ high-entropy alloys in simulated seawater environment, Corros. Sci. 111530 (2023), https://doi.org/10.1016/j.corsci.2023.111530.

[24] Y.K. Cao, Y. Liu, B. Liu, et al., Effects of Al and Mo on high temperature oxidation behavior of refractory high entropy alloys, Trans. Nonferrous Metals Soc. China 29 (2019) 1476–1483, https://doi.org/10.1016/S1003-6326(19)65054-5.

[25] S.N. Lekakh, O. Neroslavsky, M. Li, et al., Effect of spallation on oxidation kinetics of heat-resistant Cr–Ni austenitic steels on air and combustion atmosphere, High Temperat. Corros. Mater. 99 (2023) 79–99, https://doi.org/10.1007/s11085-022-10139-x.

[26] C.O. Moon, S.B. Lee, Analysis on failures of protective-oxide layers and cyclic oxidation, Oxid. Met. 39 (1993) 1–13.

[27] T.M. Butler, K.J. Chaput, Native oxidation resistance of $Al_{20}Nb_{30}Ta_{10}Ti_{30}Zr_{10}$ refractory complex concentrated alloy (RCCA), J. Alloys Compd. 787 (2019) 606–617, https://doi.org/10.1016/j.jallcom.2019.02.128.

[28] C.M. Liu, H.M. Wang, S.Q. Zhang, et al., Microstructure and oxidation behavior of new refractory high entropy alloys, J. Alloys Compd. 583 (2014) 162–169, https://doi.org/10.1016/j.jallcom.2013.08.102.

[29] S. Lu, X. Li, X. Liang, et al., Effect of V and Ti on the oxidation resistance of WMoTaNb refractory high-entropy alloy at high temperatures, Metals 12 (2022), https://doi.org/10.3390/met12010041.

[30] O.N. Senkov, S.V. Senkova, D.M. Dimiduk, et al., Oxidation behavior of a refractory $NbCrMo_{0.5}Ta_{0.5}TiZr$ alloy, J. Mater. Sci. 47 (2012) 6522–6534, https://doi.org/10.1007/s10853-012-6582-0.

[31] R. Su, H. Zhang, G. Ouyang, et al., Oxidation mechanism in a refractory multiple-principal-element alloy at high temperature, Acta Mater. 246 (2023) 118719, https://doi.org/10.1016/j.actamat.2023.118719.

[32] F. Xu, X. Gao, H. Cui, et al., Lightweight and high hardness (AlNbTiVCr)100-xNi_x high entropy alloys reinforced by laves phase, Vacuum 213 (2023), https://doi.org/10.1016/j.vacuum.2023.112115.

[33] S. Wu, D. Qiao, H. Zhang, et al., Microstructure and mechanical properties of $C_xHf_{0.25}NbTaW_{0.5}$ refractory high-entropy alloys at room and high temperatures, J. Mater. Sci. Technol. 97 (2021) 229–238, https://doi.org/10.1016/j.jmst.2021.05.015.

[34] M. Wang, Z.L. Ma, Z.Q. Xu, et al., Effects of vanadium concentration on mechanical properties of $V_xNbMoTa$ refractory high-entropy alloys, Mater. Sci. Eng. A 808 (2021) 1–8, https://doi.org/10.1016/j.msea.2021.140848.

[35] J. Li, X. Yang, R. Zhu, et al., Corrosion and serration behaviors of $TiZr_{0.5}NbCr_{0.5}V_xMo_y$ high entropy alloys in aqueous environments, Metals 4 (2014) 597–608, https://doi.org/10.3390/met4040597.

[36] C. Nyby, X. Guo, J.E. Saal, et al., Electrochemical metrics for corrosion resistant alloys, Sci. Data 8 (2021) 58, https://doi.org/10.1038/s41597-021-00840-y.

[37] Z. Wang, Y. Yan, Y. Wu, et al., Corrosion and tribocorrosion behavior of equiatomic refractory medium entropy TiZr(Hf, ta, Nb) alloys in chloride solutions, Corros. Sci. 199 (2022) 110166, https://doi.org/10.1016/j.corsci.2022.110166.

[38] K. Patel, M. Sadeghilaridjani, M. Pole, et al., Hot corrosion behavior of refractory high entropy alloys in molten chloride salt for concentrating solar power systems, Sol. Energy Mater. Sol. Cells 230 (2021) 111222, https://doi.org/10.1016/j.solmat.2021.111222.

[39] J. Jayaraj, C. Thinaharan, S. Ningshen, et al., Corrosion behavior and surface film characterization of TaNbHfZrTi high entropy alloy in aggressive nitric acid medium, Intermetallics 89 (2017) 123–132, https://doi.org/10.1016/j.intermet.2017.06.002.

[40] Y. Qiu, S. Thomas, M.A. Gibson, et al., Microstructure and corrosion properties of the low-density single-phase compositionally complex alloy AlTiVCr, Corros. Sci. 133 (2018) 386–396.

[41] K.C. Lo, Y.J. Chang, H. Murakami, et al., An oxidation resistant refractory high entropy alloy protected by CrTaO4 -based oxide, Sci. Rep. 9 (2019) 3–4, https://doi.org/10.1038/s41598-019-43819-x.

[42] Y. Du, D. Ding, L. Lai, et al., Effect of Y on the high-temperature oxidation behavior of CrMoTaTi refractory high entropy alloy, Int. J. Refract. Met. Hard Mater. 103 (2022) 1–11, https://doi.org/10.1016/j.ijrmhm.2021.105755.

[43] Y. Xiao, W. Kuang, Y. Xu, et al., Microstructure and oxidation behavior of the CrMoNbTaV high-entropy alloy, J. Mater. Res. 34 (2019) 301–308, https://doi.org/10.1557/jmr.2018.340.

[44] T.M. Butler, K.J. Chaput, J.R. Dietrich, et al., High temperature oxidation behaviors of equimolar NbTiZrV and NbTiZrCr refractory complex concentrated alloys (RCCAs), J. Alloys Compd. 729 (2017) 1004–1019, https://doi.org/10.1016/j.jallcom.2017.09.164.

[45] ASTM E92-17, E92–17 Standard Test Methods for Vickers Hardness and Knoop Hardness of Metallic Materials, ASTM International, 2009.

[46] ASTM G59-97 standard test method for conducting Potentiodynamic polarization resistance measurements, ASTM Int. 97 (2020).

[47] O.N. Senkov, S.V. Senkova, C. Woodward, et al., Low-density, refractory multi-principal element alloys of the Cr-Nb-Ti-V-Zr system: microstructure and phase analysis, Acta Mater. 61 (2013) 1545–1557, https://doi.org/10.1016/j.actamat.2012.11.032.

[48] J. Yi, S. Tang, C. Zhang, et al., Microstructure and mechanical properties of a new refractory equiatomic CrHfNbTaTi high-entropy alloy, JOM 73 (2021) 934–940, https://doi.org/10.1007/s11837-020-04557-y.

[49] T.M. Butler, O.N. Senkov, M.A. Velez, et al., Microstructures and mechanical properties of CrNb, CrNbTi, and CrNbTaTi concentrated refractory alloys, Intermetallics 138 (2021) 107323, https://doi.org/10.1016/j.intermet.2021.107323.

[50] M. Tsai, J. Yeh, High-entropy alloys: a critical review, Mater. Res. Lett. 2 (2014) 107–123, https://doi.org/10.1080/21663831.2014.912690.

[51] D.K. Ganji, G. Rajyalakshmi, Influence of alloying compositions on the properties of nickel-based superalloys: A review, in: Lecture Notes in Mechanical Engineering, Springer Science and Business Media Deutschland GmbH, 2020, pp. 537–555, https://doi.org/10.1007/978-981-15-1071-7_44.

[52] S.H. Chen, J.S. Zhang, S. Guan, et al., Microstructure and mechanical properties of $WNbMoTaZr_x$ (x = 0.1, 0.3, 0.5, 1.0) refractory high entropy alloys, Mater. Sci. Eng. A 835 (2022) 1–10.

[53] Y. Chen, G. Xiao, Y. Ji, et al., Effects of Zr content on the microstructure and performance of $TiMoNbZr_x$ high-entropy alloys, Metals 11 (2021) 1–12, https://doi.org/10.3390/met11081315.

[54] M. Wang, Z.L. Ma, Z.Q. Xu, et al., Designing $V_xNbMoTa$ refractory high-entropy alloys with improved properties for high-temperature applications, Scr. Mater. 191 (2021) 131–136, https://doi.org/10.1016/j.scriptamat.2020.09.027.

[55] V.P. Parkhutik, Oscillations of open-circuit potential during immersion plating of silicon in CuSO4/HF solutions, Russ. J. Electrochem. 42 (2006), https://doi.org/10.1134/S1023193506050090.

[56] Z.J. Zheng, Y. Gao, Y. Gui, et al., Corrosion behaviour of nanocrystalline 304 stainless steel prepared by equal channel angular pressing, Corros. Sci. 54 (2012) 60–67, https://doi.org/10.1016/j.corsci.2011.08.049.

[57] P. Murmey, U. Nichul, M. Chikode, et al., Effect of post-processing on corrosion behavior of LPBF built inconel 718 alloy, JOM 75 (2023) 32–44, https://doi.org/10.1007/s11837-022-05565-w.

[58] D. Kumar, O. Maulik, V.K. Sharma, et al., Understanding the effect of tungsten on corrosion behavior of $AlCuCrFeMnW_x$ high-entropy alloys in 3.5 wt% NaCl solution, J. Mater. Eng. Perform. 27 (2018) 4481–4488, https://doi.org/10.1007/s11665-018-3536-y.

[59] N. Razumov, T. Makhmutov, A. Kim, et al., Refractory CrMoNbWV high-entropy alloy manufactured by mechanical alloying and spark plasma sintering: evolution of microstructure and properties, Materials 14 (2021) 1–14, https://doi.org/10.3390/ma14030621.

[60] L. Wei, W. Qin, Corrosion mechanism of eutectic high-entropy alloy induced by micro-galvanic corrosion in sulfuric acid solution, Corros. Sci. 206 (2022), https://doi.org/10.1016/j.corsci.2022.110525.

[61] R. Zhang, J. Meng, J. Han, et al., Oxidation resistance properties of refractory high-entropy alloys with varied $Al_xCrTiMo$ content, J. Mater. Sci. 56 (2021) 1–11, https://doi.org/10.1007/s10853-020-05480-y.

[62] R. Romero, I.J. Beyerlein, C.V. Ramana, Microstructure and oxidation behavior of a CrMoNbTaW refractory high entropy alloy, ACS Appl. Eng. Mater. 1 (2023) 132–139, https://doi.org/10.1021/acsaenm.2c00025.

[63] O.N. Senkov, C.F. Woodward, Microstructure and properties of a refractory $NbCrMo_{0.5}Ta_{0.5}TiZr$ alloy, Mater. Sci. Eng. A 529 (2011) 311–320, https://doi.org/10.1016/j.msea.2011.09.033.

[64] L. Brewer, Prediction of transition metal phase diagrams, J. Nucl. Mater. 51 (1974) 2–11.

[65] S. Guo, C. Ng, J. Lu, et al., Effect of valence electron concentration on stability of fcc or bcc phase in high entropy alloys, J. Appl. Phys. 103505 (2011) 1–6, https://doi.org/10.1063/1.3587228.

[66] X. Yang, Y. Zhang, Prediction of high-entropy stabilized solid-solution in multi-component alloys, Mater. Chem. Phys. 132 (2012) 233–238, https://doi.org/10.1016/j.matchemphys.2011.11.021.

[67] B.Y. Zhang, Y.J. Zhou, J.P. Lin, et al., Solid-solution phase formation rules for multi-component alloys, Adv. Eng. Mater. 10 (2008) 534–538, https://doi.org/10.1002/adem.200700240.

[68] M. Zhang, X. Zhou, J. Li, Microstructure and mechanical properties of a refractory CoCrMoNbTi high-entropy alloy, J. Mater. Eng. Perform. 26 (2017) 3657–3665, https://doi.org/10.1007/s11665-017-2799-z.

[69] J.C. Phillips, Heats of formation of interstitial compounds and their alloys, J. Phys. Chem. Solids 34 (1973), https://doi.org/10.1016/S0022-3697(73)80012-5.

[70] A.K. Singh, A. Subramaniam, On the formation of disordered solid solutions in multi-component alloys, J. Alloys Compd. 587 (2014) 113–119, https://doi.org/10.1016/j.jallcom.2013.10.133.
[71] H.A. Aly, K.A. Abdelghafar, G.A. Gaber, et al., Fabrication, characterization, and corrosion behavior of a new $Cu_{40}Mn_{25}Al_{20}Fe_5Co_5Ni_5$ high-entropy alloy in HNO_3 solution, J. Mater. Eng. Perform. 30 (2021) 1430–1443, https://doi.org/10.1007/s11665-020-05390-9.
[72] C. Xiang, H.M. Fu, Z.M. Zhang, et al., Effect of Cr content on microstructure and properties of $Mo_{0.5}VNbTiCr_x$ high-entropy alloys, J. Alloys Compd. 818 (2020), https://doi.org/10.1016/j.jallcom.2019.153352.
[73] L. Fang, J. Wang, X. Li, et al., Effect of Cr content on microstructure characteristics and mechanical properties of $ZrNbTaHf_{0.2}Cr_x$ refractory high entropy alloy, J. Alloys Compd. 924 (2022) 166593, https://doi.org/10.1016/j.jallcom.2022.166593.
[74] O.N. Senkov, S.V. Senkova, C. Woodward, et al., Low-density, refractory multi-principal element alloys of the Cr–Nb–Ti–V–Zr system: microstructure and phase analysis, Acta Mater. 61 (2013) 1545–1557, https://doi.org/10.1016/j.actamat.2012.11.032.
[75] N. Yurchenko, N. Stepanov, G. Salishchev, Laves-phase formation criterion for high-entropy alloys, Mater. Sci. Technol. 33 (2017) 1153277, https://doi.org/10.1080/02670836.2016.1153277.
[76] C.B. Nascimento, U. Donatus, C.T. Ríos, et al., A review on corrosion of high entropy alloys: exploring the interplay between corrosion properties, alloy composition, passive film stability and materials selection, Mater. Res. 25 (2022) 1–16, https://doi.org/10.1590/1980-5373-MR-2021-0442.
[77] O. Swanson, Corrosion of High-Entropy Alloys in Chloride Solutions, Graduate School of The Ohio State University, 2018.
[78] G.S. Frankel, T. Li, J.R. Scully, Perspective—localized corrosion: passive film breakdown vs pit growth stability, J. Electrochem. Soc. 164 (2017) C180–C181, https://doi.org/10.1149/2.1381704jes.
[79] D.E. Williams, Y. Yang, E.G. Webb, et al., Explanation for initiation of pitting corrosion of stainless steels at sulfide inclusions, J. Electrochem. Soc. 147 (2000) 1763–1766, https://doi.org/10.1149/1.1393431.
[80] P. Wang, Y. Wang, F. Cui, et al., Microstructural evolution, mechanical properties and corrosion resistance of $CoCrFeNiW_{0.5}$ high entropy alloys with various annealing heat treatment, J. Alloys Compd. 918 (2022), https://doi.org/10.1016/j.jallcom.2022.165602.
[81] C. Liu, Y. Gao, K. Chong, et al., Effect of Nb content on the microstructure and corrosion resistance of $FeCoCrNiNb_x$ high-entropy alloys in chloride ion environment, J. Alloys Compd. 935 (2023), https://doi.org/10.1016/j.jallcom.2022.168013.
[82] Z. Peng, B. Li, Z. Luo, et al., A lightweight $AlCrTiV_{0.5}Cu_x$ High-entropy alloy with excellent corrosion resistance, Materials 16 (2023) 2922, https://doi.org/10.3390/ma16072922.
[83] B.M. Hunter, Oxidation Behavior of Refractory Complex Concentrated Alloys: Computational and Experimental Studies, University of Alabama, Thesis, 2019.
[84] X. Zhang, X. Cui, G. Jin, et al., Microstructure evolution and performance enhancement of NbTaTiV-(Cr, Zr, W) single-phase refractory high-entropy alloy coatings: role of additional elements, J. Alloys Compd. 951 (2023) 169918, https://doi.org/10.1016/j.jallcom.2023.169918.
[85] Y. Du, D. Ding, L. Lai, et al., Effect of Y on the high-temperature oxidation behavior of CrMoTaTi refractory high entropy alloy, Int. J. Refract. Met. Hard Mater. 103 (2022), https://doi.org/10.1016/j.ijrmhm.2021.105755.
[86] A.O. Moghaddam, M. Sudarikov, N. Shaburova, et al., High temperature oxidation resistance of W-containing high entropy alloys, J. Alloys Compd. 897 (2022) 1–10, https://doi.org/10.1016/j.jallcom.2021.162733.
[87] Q.Q. Hou, K. Huang, L.M. Luo, et al., Microstructure and its high temperature oxidation behavior of W-Cr alloys prepared by spark plasma sintering, Materialia 6 (2019) 100332, https://doi.org/10.1016/j.mtla.2019.100332.
[88] S. Sheikh, M.K. Bijaksana, A. Motallebzadeh, et al., Accelerated oxidation in ductile refractory high-entropy alloys, Intermetallics 97 (2018) 58–66, https://doi.org/10.1016/j.intermet.2018.04.001.
[89] S. Abbaszadeh, A. Pakseresht, H. Omidvar, et al., Investigation of the high-temperature oxidation behavior of the $Al_{0.5}CoCrFeNi$ high entropy alloy, Surf. Interf. 21 (2020) 100724, https://doi.org/10.1016/j.surfin.2020.100724.
[90] X. Yang, Z. Zeng, X. Wang, et al., High-temperature oxidation behaviors of 321 steel with Y or Nb micro-alloying, Crystals 13 (2023) 781, https://doi.org/10.3390/cryst13050781.
[91] L. Zheng, M. Zhang, R. Chellali, et al., Investigations on the growing, cracking and spalling of oxides scales of powder metallurgy Rene95 nickel-based superalloy, Appl. Surf. Sci. 257 (2011) 9762–9767, https://doi.org/10.1016/j.apsusc.2011.06.005.
[92] Y. Yan, K.A. McGarrity, D.J. Delia, et al., The oxidation-resistance mechanism of WTaNbTiAl refractory high entropy alloy, Corros. Sci. 204 (2022) 110377, https://doi.org/10.1016/j.corsci.2022.110377.
[93] O.S. Bamisaye, N. Maledi, J. Van der Merwe, M.O. Bodunrin, Microstructure, hardness, oxidation, and corrosion behavior of TiNbTaVW refractory high entropy alloy in 3.5 wt% NaCl and 1 M H_2SO_4, J. Alloys Compd. 983 (2024) 173803, https://doi.org/10.1016/j.jallcom.2024.173803.
[94] R. Mevrel, Cyclic oxidation of high-temperature alloys, Mater. Sci. Technol. 3 (1986) 531–535, https://doi.org/10.1080/02670836.1987.11782264.
[95] H. Jeong, S.H. Kim, W.S. Choi, et al., Spallation resistance of oxide scales on alloy 617 enhanced by boron addition, Corros. Sci. 140 (2018) 196–204, https://doi.org/10.1016/j.corsci.2018.06.002.
[96] J. Kuang, P. Zhang, Q. Wang, Z. Hu, X. Liang, B. Shen, Formation and oxidation behavior of refractory high-entropy silicide $(NbMoTaW)Si_2$ coating, Corros. Sci. 198 (2022) 110134, https://doi.org/10.1016/j.corsci.2022.110134.
[97] B. Panicaud, J.L. Grosseau-Poussard, J.F. Dinhut, On the growth strain origin and stress evolution prediction during oxidation of metals, Appl. Surf. Sci. 252 (2006) 5700–5713, https://doi.org/10.1016/j.apsusc.2005.07.075.
[98] F. Song, B.E. White, Growth of Ultra-Thin Vanadium Dioxide Thin Films Using Magnetron Sputtering, 2016, p. 03911. http://arxiv.org/abs/1608.03911.
[99] Y. Zhu, Y. Zhang, F.C. Cheong, et al., Annealing effects on the elastic modulus of tungsten oxide nanowires, J. Mater. Res. 23 (2008) 2149–2156, https://doi.org/10.1557/jmr.2008.0277.
[100] E. Besozzi, D. Dellasega, V. Russo, et al., Thermomechanical properties of amorphous metallic tungsten-oxygen and tungsten-oxide coatings, Mater. Des. 165 (2019) 107565, https://doi.org/10.1016/j.matdes.2018.107565.